UC Irvine

UC Irvine Electronic Theses and Dissertations

Title

Shrink-Induced Silica Structures for Improved Biological Detection

Permalink

https://escholarship.org/uc/item/5tk335xm

Author

Lin, Sophia

Publication Date

2016

Peer reviewed|Thesis/dissertation

eScholarship.org Powered by the California Digital Library
University of California

UNIVERSITY OF CALIFORNIA,
IRVINE

Shrink-Induced Silica Structures for Improved Biological Detection

DISSERTATION

submitted in partial satisfaction of the requirements
for the degree of

DOCTOR OF PHILOSOPHY

in Chemical Engineering & Materials Sciences

by

Sophia Lin

Dissertation Committee:
Associate Professor Michelle Khine, Chair
Professor Albert Yee
Assistant Professor Jered Haun

2016

Portion of Chapter 1 © 2004 Nature Publishing Group and Copyright Clearance Center

Portion of Chapter 2 © 2014 The Royal Society of Chemistry

Portion of Chapter 3 © 2014 The Royal Society of Chemistry

Portion of Chapter 3 © 2009 John Wiley and Sons and Copyright Clearance Center

Portion of Chapter 4 © 2013 John Wiley and Sons and Copyright Clearance Center

Portion of Chapter 5 © 2013 John Wiley and Sons and Copyright Clearance Center

Portion of Chapter 6 © 2013 John Wiley and Sons and Copyright Clearance Center

All other materials © 2016 Sophia Lin

DEDICATION

To

my parents Wun-Jin Lin and Sheau-Uan Jiang

my brother Eugene Lin

TABLE OF CONTENTS

LIST OF FIGURES

LIST OF TABLES

ACKNOWLEDGMENTS

I would like to express my deepest gratitude to my academic advisor Professor Michelle Khine for her mentorship and guidance throughout the years. I ended up working for Michelle partly by chance as I was only able to catch her (in between all her meetings!) by parking myself in front of her office one afternoon, and it was probably the best hour of waiting I have invested in. She is a remarkable role model, and her energy, enthusiasm, and overall grit inspire and motivate all those who work with her. She has one of the biggest hearts I know, and I am eternally grateful for all that she has done for me. I thank her for challenging and pushing me because without her, I would not be who I am today.

I would like to thank my committee members, Professor Albert Yee and Professor Jered Haun, for their questions and thoughtful suggestions. I also would like to thank Professor Vasan Venupagalan, with whom I have had fruitful discussions about my work. I would like to thank Dr Enrico Gratton and Dr. Per Niklas for his help and intelligent contribution to my project.

I would like to thank Neil Sahota for the many real life examples he has provided for someone who so far has only known the Ivory Tower of academia. I also thank him for his confidence and mentorship throughout the NSF I-Corps L program, one of the most challenging experiences of my graduate career.

I would like to thank all the members of the Khine lab past and present, especially Dr. Aaron Chen, Dr. Himanshu Sharma, Dr. Jolie McLane Nokes, Jon Pegan, Eugene Lee, and Roger Tu for making the lab feel more like a home, and work feel more like play. I have always benefited from their perspectives.

I also would like to thank all the friends that I have made during my time at UCI as they have deeply enriched my life. From running plays with the ChEMS intramural football team to rappelling down the side of a mountain with friends from the rock-climbing gym, I have done things I would have never imagined.

I would like to thank David Tran for his patience, optimism, and encouragement in all my endeavors. And for making all our shared adventures that much better.

Lastly, I would like to express my deepest appreciation to my family. I would like to thank my brother Eugene Lin, for the good food and laughter during our residency in Irvine. I would like to thank my mom and dad for their eternal support and unconditional acceptance in all that I choose to do.

I am grateful for all the opportunities and experiences I have had at my time at UCI and all the people I have met along the way. They have shaped who I am today.

This work was supported by the National Institute of Health (NIH) through DP NIH Director's New Innovator Award (1 DP2 OD007283-01) and the National Science Foundation (NSF)

Biophotonics across Energy, Space, and Time (BEST) Integrative Graduate Education Research Traineeship (IGERT).

CURRICULUM VITAE

Sophia Lin

2016	**PhD**, University of California, Irvine Chemical Engineering & Materials Science *Thesis*: Shrink-Induced Silica Structures for Improved Biological Detection
2012	**MS**, University of California, Irvine Chemical Engineering & Materials Science
2010	**BS**, University of California, Los Angeles Chemical and Biomolecular Engineering

PUBLICATIONS

S. Lin, P.N. Hedde, V. Venupagalon, E. Gratton, and M. Khine, "Multi-scale silica structures for improved HIV-1 Capsid (p24) antigen detection," *In preparation.*

H. Sharma, J. Wood, S. Lin, R. Corn, and M. Khine, "Shrink-induced silica multiscale structures for enhanced fluorescence from DNA microarrays," *Langmuir*. 2014, 10.1021/la501123b

S. Lin, E. Lee, N. Nguyen and M. Khine, "Thermally-induced miniaturization for micro- and nanofabrication: progress and updates," *Lab Chip*. 2014, 10.1039/C4LC00528G

S. Lin, H. Sharma, and M. Khine, "Silica nanostructures: Shrink-induced silica structures for far-field fluorescence enhancements," *Adv. Opt. Mater*., 1:567. Doi:10.1002/adom.201370051 (Accepted June 2013 as Frontispiece)

ORAL PRESENTATIONS

S. Lin, E. Lee, J. Pegan, H. Sharma, and M. Khine "SMART (Shrink Manufacturing Advanced Research Tools)," Transducers 2015, Anchorage, Alaska, June 2015

S. Lin, H. Sharma, and M. Khine, "Silica structures for fluorescence detection of biologicals", Southern California Micro and Nanofluidics Symposium, Pasadena, California, June 2015

H. Sharma, J. Wood, S. Lin, R. Corn, and M. Khine, "Shrink Wrap Multi-scale Silica Structures Used to Enhance Fluorescence Detection for DNA Microarrays", Biomedical Engineering Society (BMES), San Antonio, Texas, October 2014

H. Sharma, J. Wood, S. Lin, R. Corn, and M. Khine, "Shrink Wrap Multi-scale Silica Structures Used to Enhance Fluorescence Detection for DNA Microarrays", The Annual UC Systemwide Bioengineering Symposium, Irvine, California, June 2014

S. Lin, H. Sharma, J. McLane, N. Norouzi, and M. Khine, "Rapid shrink-induced production of micro- and nanostructures for enhanced fluorescence detection", The Annual UC Systemwide Bioengineering Symposium, Berkeley, California, June 2012

POSTER PRESENTATIONS

S. Lin and M. Khine, "Silica structures for enhanced fluorescence detection", Center for Advanced Design and Manufacturing of Integrated Microfluidics (CADMIM) Planning Meeting, Irvine, California, May 2015

S. Lin and M. Khine, "Silica structures for enhanced fluorescence detection", IEEE-EMBS Micro- and Nanoengineering in Medicine Conference, Oahu, Hawaii, December 2014

S. Lin, M. Rahim, J. Jaun, and M. Khine, "Silica Structures for Enhanced Far-field Protein Detection", The Annual UC Systemwide Bioengineering Symposium, Irvine, California, June 2014

H. Sharma, S. Lin, J. Wood, R. Corn, and M. Khine, "Shrink-Induced Multi-scale Silica Structures for Enhanced Fluorescence Detection", Center for Advanced Design and Manufacturing of Integrated Microfluidics (CADMIM) Planning Meeting, Irvine, California, May 2014

S. Lin, H. Sharma, P. Kahn, and M. Khine, "Rapid Shrink-Induced Production of Silica Structures for Fluorescence Enhancements", Center for Advanced Design and Manufacturing of Integrated Microfluidics (CADMIM) Planning Meeting, Irvine, California, May 2013

S. Lin, H. Sharma, P. Kahn, and M. Khine, "Rapid Shrink-Induced Production of Silica Structures for Fluorescence Enhancements", IEEE-EMBS Micro- and Nanoengineering in Medicine Conference, Ka'anapali, Hawaii, December 2012

S. Lin, H. Sharma, J. McLane, N. Norouzi, and M. Khine, "Ultra-rapid shrink-induced enhanced fluorescence detection with SiO_2 micro- and nanostructured substrate", Biomedical Engineering Society (BMES) Annual Meeting, Atlanta, Georgia, October 2012

S. Lin, H. Sharma, J. McLane, N. Norouzi, and M. Khine, "Ultra-rapid shrink-induced enhanced fluorescence detection with SiO_2 micro- and nanostructured substrate", Bringing Diagnostic Prototypes to the Point of Care, Nairobi, Kenya, June 2012

HONORS AND AWARDS

2015	NSF I-corps L Entrepreneurial Lead, UCI
2015	Chancellor's Club Fellow, UCI
2015	Honorable Mention, Public Impact Fellow, UCI
2013 – 2015	NSF Biophotonics across Energy, Space, and Time (BEST) Interdisciplinary Graduate Education and Research Traineeship (IGERT), UCI

2010 – 2011 Graduate Assistance in Areas of National Need (GAANN) Fellowship, UCI

ABSTRACT OF THE DISSERTATION

Shrink-Induced Silica Structures for Improved Biological Detection

By

Sophia Lin

Doctor of Philosophy in Chemical Engineering and Materials Sciences

University of California, Irvine, 2016

Associate Professor Michelle Khine, Chair

Routine surveillance for infectious diseases results in earlier detection and better prognosis. However, current diagnostic measures for infectious diseases are not directly translatable to low-resource settings as they are expensive, time-consuming, and require heavy medical infrastructure and trained personnel. The need for effective point-of-care (POC) diagnostics is critically important: the vast majority of deaths from infectious diseases occur in developing countries.

Here, a platform for producing enhanced fluorescence signals with applications in POC technology is presented. Dense multi-scale silica (SiO_2) structures are fabricated on pre-stressed polyolefin (PO) film and characterized. Linkage of fluorescent biomolecules on the SiO_2 structures results in far-field fluorescence signal enhancements (~116-fold with respect to a planar glass control and ~50-fold with respect to a flat unshrunk fluorescently conjugated polymer film) with increased signal-to-noise ratio (SNR) that are robust and reproducible. Optical characterization of the SiO_2 structures point to the concentration effect and optical scattering as the underlying mechanisms responsible for the far-field fluorescence signal enhancements.

Using the biotin-streptavidin hybridization as a model system, improved limits of detection (LOD) of the model target streptavidin were achieved on the SiO_2 structures relative to a flat glass control. Disease detection applications are demonstrated using the SiO_2 structures. Sandwich immunoassays for TNF-α and p24 antigen are performed on the SiO_2 structures and lower LODs are achieved (550 pg mL^{-1} and 30 pg mL^{-1} for TNF-α and p24 antigen, respectively). The SiO_2 structures demonstrate potential for POC applications as enhanced signal correlates to increased sensitivity.

CHAPTER 1: INTRODUCTION

1.1 Motivation

Infectious diseases result in approximately 15 million deaths a year, collectively the second leading cause of deaths worldwide.[1] Despite advancements in countermeasures such as diagnostics, therapeutics, and vaccines, infectious diseases remain prevalent not only due to human activity such as global interdependence and world travel, but also due to microbial evolution and antibiotic resistance. Examples of modern infectious diseases (both newly emerging and re-emerging) are shown in **Figure 1.1**; these include HIV/AIDS, H1N1 influenza, malaria, severe, and diarrheal diseases.[2]

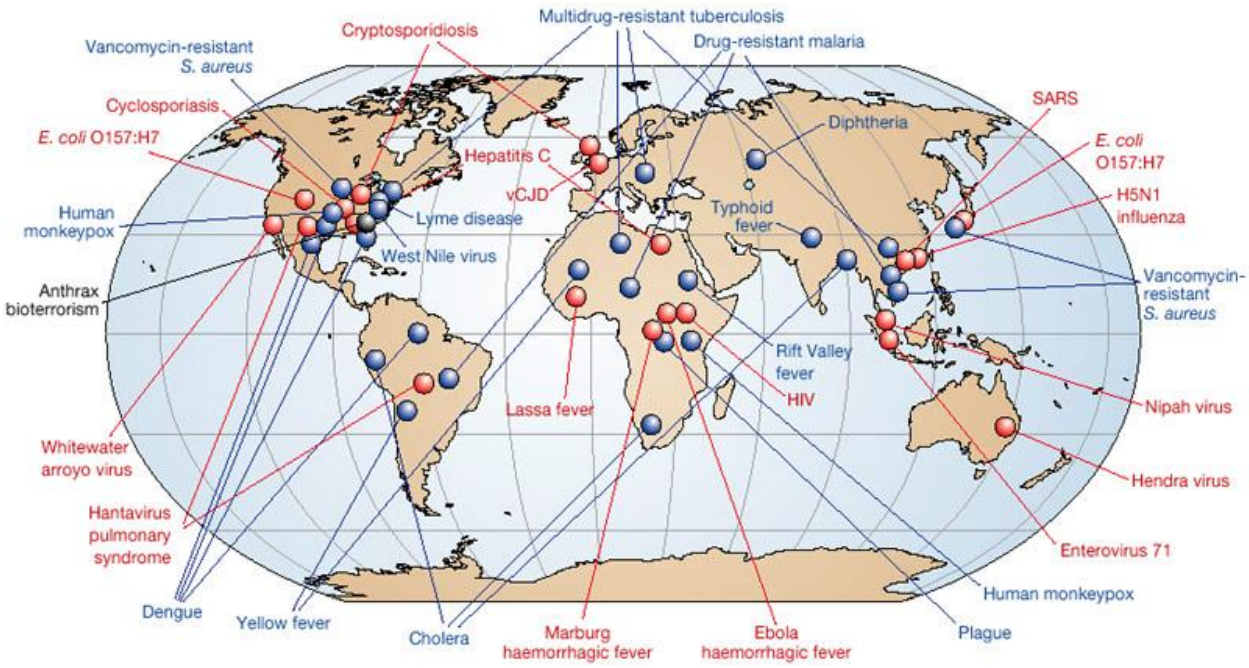

Figure 1.1 Schematic illustration depicting newly emerging and re-emerging infectious diseases that occur globally, where the blue text represents re-emerging infectious diseases, the red text represents newly emerging diseases, and the black text represents a 'deliberately' emerging disease.[2] Reprinted by permission from Macmillan Publishers Ltd: Nature *430* (6996), 242–249, © (2004).

Diagnosis of infectious diseases is traditionally done through microbial cultures, serology, microscopy, and more recently, molecular diagnostics.[3–5] The diagnostic process in regions with readily accessible health care facilities usually involves patient check-in, physician examination, pathological testing, and sample analysis. The turn-around time for a diagnosis ranges from hours to days.[6,7] This process is not easily translatable to low-resource settings that suffer from lack of accurate diagnostic tools and weak healthcare infrastructure. Typically, these diagnostic methods are also far too expensive and treatment is merely based off of clinical symptoms. The fact that over 95% of deaths due to infectious diseases occur in developing countries further highlights a need for rapid, inexpensive, portable, and accurate method for disease diagnosis.[8,9] This would not only enable individual treatment, but timely diagnosis also is crucial for global surveillance and disease control. Therefore, a need exists for effective point-of-care (POC) devices. POC diagnostics are generally described as tests that do not require laboratory staff or facilities to provide a timely result at the patient's site.[10] They should, as the World Health Organization (WHO) set forth, be "ASSURED" (Affordable, Sensitive, Specific, User-friendly, Robust, Equipment-free, and Deliverable).[4,11]

Most existing POC diagnostics for infectious diseases are based on antigen-antibody binding in the form of lateral flow assays (LFA) or rapid diagnostic tests (RDT).[5] While many POC diagnostics are simple, cheap to fabricate, and require little equipment, on-going research to develop technologies for lower limits of detection (LOD) persist. Detecting lower LOD at an earlier stage can potentially allow for earlier diagnosis and containment. Improvements to POC technologies are crucial. This work aims to develop a POC technology for enhanced detection of surface bound analytes using optical readout methods.

1.2 Dissertation overview

This dissertation is structured as follows. Chapter 2 gives a brief background to fluorescence phenomenon, characterization typically done regarding fluorescence samples, introduces the need for improved fluorescence sensing, and our proposed alternative towards improving fluorescence signal detection. Chapter 3 introduces the shrink technology platform as a fabrication method for multiscale micro- and nano- structures, and characterizes the tunable micro- to nanostructures generated using the shrink technology. In Chapter 4, we demonstrate proof-of-concept on the wrinkled structures that indicates potential of our platform for improved diagnostic capability. We characterize the tunable wrinkles to understand the optical properties and the mechanisms arising from the enhanced detection capabilities achieved on the wrinkles in Chapter 5. We then show clinical applicability of our platform through improved detection limits in Chapter 6. We conclude with a discussion of future directions and some work done in this area in Chapter 7.

CHAPTER 2: FLUORESCENCE AND SENSING APPLICATIONS

2.1 Principles of fluorescence and characterization

Fluorescence is a natural phenomenon that has become a widely used optical read out method. Naturally occurring molecules such as aromatic amino acids, NADH, flavins, and chlorophylls exhibit intrinsic fluorescent properties.[12] When fluorescent properties are not present, extrinsic fluorescence can be induced by using fluorophores. Fluorescence is due to the absorption of a photon by an electron, its resulting transfer to a higher excited electronic state and the subsequent vibrational relaxation and energy loss that results in the emission of a photon at a longer wavelength. A simplified Jablonski diagram is shown in **Figure 2.1.** The Jablonski diagram is an energy diagram that illustrates the electronic states of a molecule and the transitions between them. Fluorescence occurs when an electron (typically at the lowest energy state) absorbs a photon with a particular energy and is transferred to a higher eigenstate. The absorbed energy can be dissipated in multiple ways, either through non-radiative or radiative processes. Non-radiative decay of a fluorophore manifests itself via processes including vibrational relaxation, internal conversion, intersystem crossing, energy transfer, and quenching. On the other hand, the energy loss can also occur through radiative decay. This involves the emission of a photon at a particular wavelength, either through fluorescence or phosphorescence, as the electron drops from the lowest singlet excited state to the ground state. The fluorescence lifetime (τ), or the time a fluorophore spends in its excited state is defined in **Equation 1**:

$$\tau = \frac{1}{k_r + k_{nr}} \quad (1)$$

Where k_r and k_{nr} are the radiative and non-radiative decay rates, respectively.

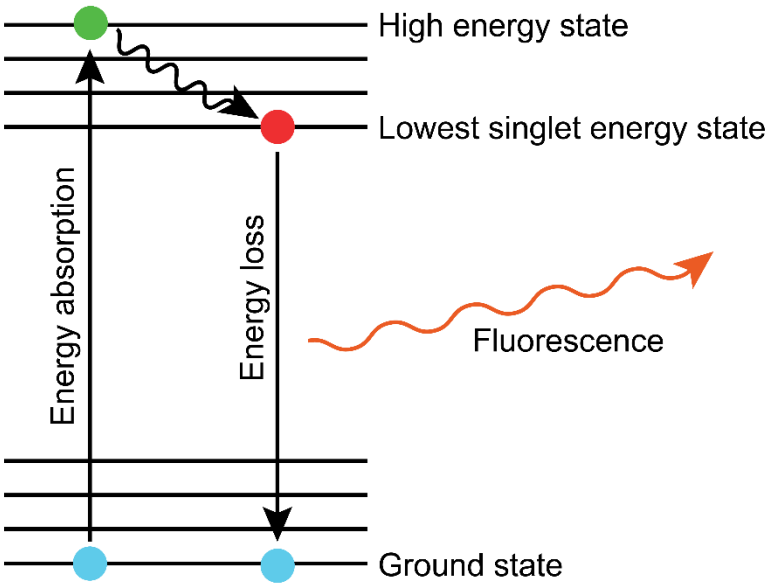

Figure 2.1 A simplified Jablonski energy diagram illustrating the absorption of a photon by an electron and its subsequent transfer to a higher excited electronic state, vibrational relaxation, and energy loss in the form of fluorescence.

To assess changes in a fluorophore's fluorescent properties, the quantum yield is typically quantified. The quantum yield (Φ) is reported as a measure of fluorescence efficiency, and is defined as the ratio of the number of photons emitted to the number absorbed. It can be expressed as shown in **Equation 2**:

$$\Phi = \frac{k_r}{k_r + k_{nr}} \qquad (2)$$

where (k_r) represents the radiative rate and (k_{nr}) represents the non-radiative rate.

For information about the fluorophore orientation, fluorescence anisotropy (r) is often measured, and is defined in **Equation 3**:

$$r = \frac{I_{\parallel} - I_{\perp}}{I_{\parallel} + 2I_{\perp}} \qquad (3)$$

Where $I_{\parallel}$ is the observed intensity when the emission polarizer is oriented parallel to the direction of the excitation and $I_{\perp}$ is the observed intensity when the emission polarizer is oriented perpendicular to the excitation. When a sample is excited with polarized light, the

molecules with absorption transitions that are aligned parallel to the electric field of the polarized excitation light have the greatest probability of being excited. This characterizes the extent of linear polarization of the fluorescence emission. Time-resolved anisotropy studies measures the depolarization of the fluorescence emission and can give insight to biomolecule mobility within its environment.[12] Lower anisotropy values indicate molecule depolarization. The schematic for fluorescence anisotropy measurements is shown in **Figure 2.2**.

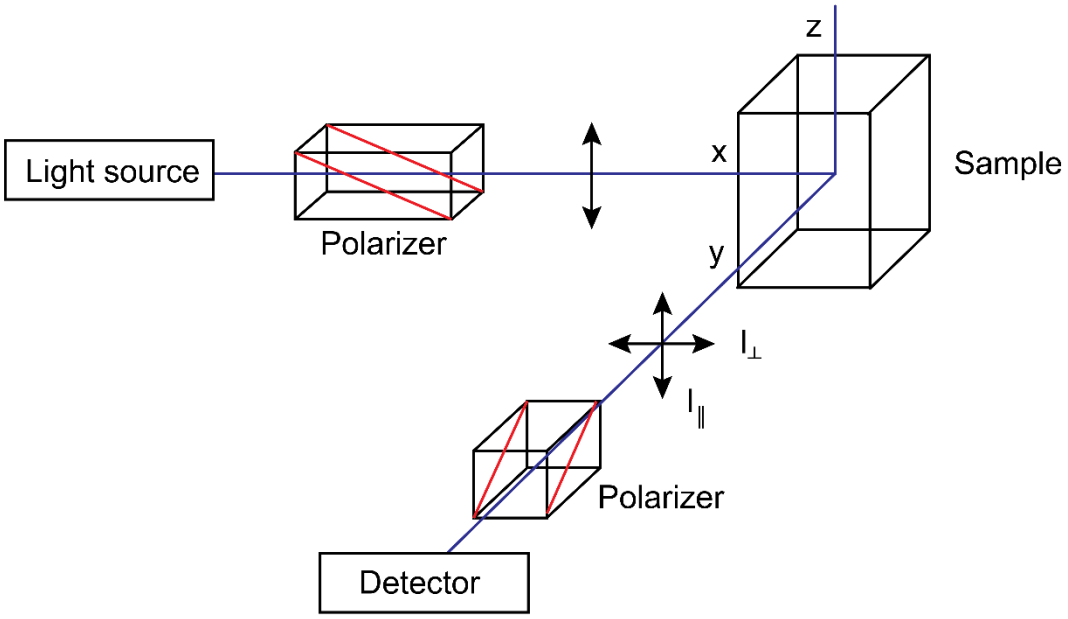

Figure 2.2. Schematic diagram for fluorescence anisotropy measurements.

2.2 A continual need for improved fluorescence signals

Fluorescence is widely used for chemical sensing,[13,14] biomolecule detection,[15,16] disease diagnostics,[17,18] and various applications in biology.[19,20] Fluorescence based detection has high levels of sensitivity, low background noise, and can be easily translated to multiplexed systems. Additionally, fluorescence based detection methods for POC technologies are further being realized with the development of field portable fluorescence microscopes.[17,21,22] Efforts to improve detection sensitivity and signal-to-noise ratios (SNRs)

of low-abundance target molecules have resulted in the development of brighter[10] and more photostable fluorescent labels,[23,24] advancements of traditional imaging devices and techniques,[25] and engineered surface structures or particles for signal enhancement.[26–28]

2.2.1 Nanostructures for enhanced fluorescence signals

One method for increasing fluorescence signals involves leveraging the localized surface plasmon resonance (LSPR) effects of metallic nanostructures or nanoparticles. This phenomenon couples light with surface plasmons for increased electromagnetic field intensity.[29,30] Increased electromagnetic field confinement enables surface enhanced Raman spectroscopy (SERS), which takes advantage of the inelastic scattering of photons and metal enhanced fluorescence (MEF) techniques, and takes advantage of the increased absorption of the local light field by a fluorophore and reduced non-radiative decay.[31,32] It has been shown that metallic nanostructures have been able to enhance averaged fluorescence signals based on MEF effects from 2-fold to up to more than 5000-fold.[33–35]

These structures, which include islands, nanoparticles, dimers, pillars, and bow-tie antennas, can be fabricated through various methods such as electrochemical growth, electron beam lithography (EBL), nanoimprint lithography (NIL), and colloidal lithography. Each method offers certain advantages, which will be briefly discussed. Metallic islands such as silver island films (SiFs) and roughened surfaces represent inhomogeneous structures that exhibit MEF effects. Fabrication of metallic islands and surfaces typically involve deposition of the metal onto an inert surface, and chemical growth of these metallic regions.[36,37] Moderate fluorescence enhancements have been reported. For example, Shtoyko *et al*. reported an average fluorescence enhancement of 7-fold with more than 100-fold

fluorescence enhancement on "hot spots" of their silver structures.[38] Zhang *et al.* reported a 7-fold and 13-fold fluorescence enhancement of Cy5 molecules on silver monomers and silver dimers relative to a Cy5-oligonucleotide in the absence of a silver particle.[39] While processing for these inhomogeneous nanostructures is relatively inexpensive, the resulting fluorescence enhancements are unpredictable and therefore do not represent a suitable platform for a diagnostic tool.

Other fabrications methods such as EBL, NIL, and colloidal lithography have yielded homogeneous metallic structures for MEF effects. Corrigan *et al*. used EBL to fabricate silver nanopillars and demonstrate tunability of the fluorescence enhancement ratio upon changing the nanopillar size and spacing. They observed up to a 20-fold increase in fluorescence enhancement factor in this systematic study.[41] Kinkhabwala *et al*. showed enhancements of 1340-fold for the near-infrared dye N,N'-bix(2,6-diisopropylphenyl)-1,6,11,16-tetra-[4-(1,1,3,3-tetramethylbutyl)phenoxyl]quaterylene-3,4:13,14-bis(dicarboximide) (TPQDI) using gold bowtie nanoantennas fabricated using EBL.[40] While EBL offers direct writing of precise structures at high resolution, it suffers from low throughput due to long write times and high cost. Alternative methods for homogeneous nanostructure fabrication that have emerged include NIL and colloidal lithography. NIL allows for large surface area (mm^2) patterning of uniform structures. It involves using a mold to imprint nanostructures into a coated substrate, removal of the mold, and additional processing steps such as reactive ion etching (RIE) for further refinement of the nanostructures.[42] Chou *et al*. showed increases of the average fluorescence intensity of immunoassay of Protein A and human IgG by over 7400-fold and uniformity of averaged fluorescence enhancement across the spatial area ($\pm$9%).[34] Das *et al.* used NIL methods to

create large-scale plasmonic 3D nanoCones structures that yielded a 10-12-fold increase fluorescence intensity for adsorbed FITC dye.[43] While NIL methods for fabricating nanostructures offer higher throughout at lower cost, they still require fabrication of the master mold (typically done with EBL), imprinting systems, and efficient delaminating processes for successful scale up. Colloidal lithography for plasmonic nanostructures relies on the close packed self-assembly of nanospheres as a shadow mask, followed by metal film deposition, and removal of the nanospheres.[44] This method also allows for large surface of uniform nanostructures. Xie *et al.* showed a 69-fold fluorescence enhancement of the near infra-red (NIR) dye Alexa Fluor 790 on gold triangles.[45] Silver triangles yielded a fluorescence enhancement factor of 83-fold for the NIR dye Alexa Fluor 790. The authors also demonstrated that by merely changing the oxygen plasma etch time, they were able to tune the plasmonic effects of the resulting silver triangles.[46] Despite the increased area of homogeneous nanostructures achievable by NIL and colloidal lithography, challenges to use these nanostructures for reliable biosensing applications persist since the plasmonic-based enhancements are typically limited to the near-field and distance dependent.

2.2.2 Silica substrates for enhanced fluorescence signals

Silica (SiO_2), otherwise known as silicon dioxide, is the oxide of silicon. It is an abundant crystalline material with applications in microelectronics, drug delivery,[47] imaging,[48] and sensors.[49–51] Silica is widely used as a sensing support because it is an optically clear, mechanically and thermally robust, and versatile surface that is amenable to many surface chemistries. Grant et al. used SiO_2 nanobeads as a platform for protease sensing applications. The increased surface area owing to the spherical geometry, optical

clarity, and surface compatibility for silane chemistry allowed for protease detection with fast response times. [51] Other groups have also leveraged these properties of SiO_2 for analyte detection. [52–54] In addition to the aforementioned characteristics that support SiO_2's use as an effective sensing platform, it has also be observed that SiO_2 can impart interesting optical effects on fluorescence, which have been leveraged for sensing applications.

In the 1990s van Blaaderen reported the direct incorporation of fluorescent molecules into SiO_2 nanospheres.[55,56] Enhanced fluorescent properties upon SiO_2 nanoparticle encapsulation has been reported. These effects not only come from increased surface area of the SiO_2 nanoparticles, which allow for increased dye loading, but enhancements of fluorescent properties are achieved through covalent encapsulation of dye into SiO_2-based nanoparticles.[57–59] Ow *et al*. reported in 2005 exceptional brightness (up to 20-fold) of their synthesized core-shell SiO_2 nanoparticles.[60] A follow up study done demonstrated that the fluorescent dye's photophysical properties changed based on the SiO_2 internal architecture.[61] Immobilization of the fluorescent dye within the SiO_2 core-shell was suggested to restrict rotational mobility, which can lead to reduced nonradiative relaxation and subsequently increased quantum yield.[61,62] SiO_2 encapsulation has also been reported to result in enhancement of radiative decay rate due to differences between the refractive index between rhodamine dyes and SiO_2 surroundings.[61–63] Since then, there have been numerous studies done encapsulating different dyes within SiO_2 nanoparticles with various degrees of fluorescence enhancements reported. [59,62,64–72] The dye doped SiO_2 nanoparticles have found applications in bioimaging, labeling, drug delivery, and diagnostic testing, and are an attractive alternative to organic fluorophores because of their low toxicity, photostability, and brightness.

2.3 The shrink platform for enhanced fluorescence

The Khine lab at UC Irvine leverages prestressed, heat-shrinkable thermoplastic polymer film for fabrication.[73] Heat-shrinkable polymer films, a type of shape memory polymer (SMP) comprised of cross-linked polymer chains, such as polyethylene,[74] poly(ethylene terephthalate),[75] and polystyrene (PS),[76] are extruded, molded, and cross-linked. The semicrystalline materials are then heated, stretched, and then cooled to "freeze in" the oriented polymer structure.[77,78] Release of the stored elastic stress and recovery to original shape occurs when the polymer film is heated past its glass transition temperature T_g.

Prior work done in the lab demonstrated the ability to increase the surface density of protein microarrays by simply pattering antibodies onto the surface of a prestressed polyolefin (PO) film and leveraging the heat-induced retraction properties of the PO sheet.[79] Biological activity of the adsorbed protein was retained despite the application of heat for substrate shrinkage, and functionality was verified through a simple fluorescence immunoassay. Modest increases in fluorescence signal (~2-fold) were observed from concentrating the biomolecules. This suggests to us the potential for improving immunoassay sensitivity by merely concentrating the number of proteins per area.[79]

2.3.1 Our strategy and project rationale

As previously discussed, nanostructures used for enhanced fluorescence signals can use expensive materials such as gold and silver, require extensive fabrication steps for precise control of homogeneous or periodic surface features, and necessitate specialized equipment (e.g. 2-photon microscopy). Importantly, while large fluorescence enhancements

have been observed, such plasmon-coupled effects suffer from practical limitations including: localized near-field effects with enhancements occurring only within nanometric lengths from the surface, heterogeneous enhancements with small areas of 'hot spots', and enhancements which are wavelength dependent. Such practical drawbacks impede progress in translating these large enhancements into solutions for deployable robust detection. Therefore, a continual need persists for a robust, low-cost, sensing platform for POC diagnostic applications.

Here we present a simple strategy to create a robust and scalable fluorescence enhancing platform based on low-cost commodity shrink wrap film. Instead of using multi-step processing techniques for fabrication of fluorescence enhancing nanostructures or dye-doped SiO_2 nanoparticles, we look to pattern at the large scale and then use the heat-shrink properties of the thermoplastic polymer film to improve fluorescence signals by bringing biomolecules closer together. We hypothesize that by covalently linking the biomolecules onto the shrinkable SiO_2 substrate, we can more efficiently conjugate biomolecules onto our PO film surface and subsequently bring the fluorescently labelled biomolecules closer together, resulting in signal concentration. This low-cost rapid method to improve the fluorescence signals is amenable to current roll-to-roll manufacturing processes and supports existing biological assays. By patterning at the large scale and then shrinking, we avoid having to deal with wetting behaviors of solutions on nanostructured surfaces and steric hindrance effects on the biomolecule binding.

CHAPTER 3: MULTISCALE STRUCTURES

3.1 Wrinkles

Micro- and nanostructures have a wide range of applications in the electrical, mechanical, biological, and optical fields. As such, much work has been done to fabricate structures at these length scales. Traditional fabrication methods for structures at the micro- and nanometer scales use techniques inherited from the semiconductor industry. While successful, these methods, such as photolithography, thin film deposition, and etching, face drawbacks such as the need for expensive cleanroom facilities and the use of harsh, environmentally damaging reagents. Resulting structures can also suffer from limited resolution and planarity. These properties hinder progress towards rapid and inexpensive scale up that many emerging applications, particularly lab-on-a-chip (LOC), necessitate.

Alternatively, soft lithography methods have been employed to fabricate wrinkles. Surface wrinkles arise from the stiffness mismatch between layered dissimilar materials. For example, elastomeric materials such as polydimethylsiloxane (PDMS) (which easily compresses and expands) can be used as a substrate for a stiff skin layer. Release of the elastomer's elastic stress causes the skin layer to buckle and fold, forming wrinkled structures.[80] A schematic is shown in **Figure 3.1**, and extensive studies have been done characterizing wrinkle formation from a bilayered materials with an elastic substrate.[81,82] The wrinkle amplitudes and wavelengths have been shown to be dependent on the thickness of the skin layer and the films' elastic properties, as shown in **Equation 4**,

$$\lambda = 2\,\pi\,h\left[\frac{\left(1-\nu_f^2\right)E_s}{3\left(1-\nu_s^2\right)E_f}\right]^{1/3} \qquad (4)$$

where h represents the thin film thickness, ν_f represents the Poisson's ratio of the thin film, ν_s represents the Poisson's ratio of the substrate, E_f represents the elastic modulus of the thin film and E_s represents the elastic modulus of the substrate. The film is also assumed to be finitely large in the lateral dimensions.

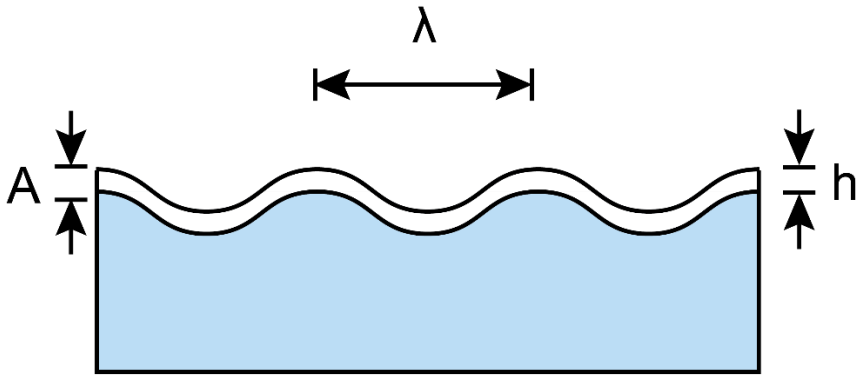

Figure 3.1 Schematic illustrating the wrinkling phenomenon, where A is the wrinkle amplitude, λ is the wavelength, and h is the skin thickness.

While PDMS has become a staple of the microfluidics community, its material properties present drawbacks such as swelling, leaching, and limited deformation.[83,84] Fabrication with PDMS is a low throughput process and is mostly used for benchtop development in a laboratory setting. These drawbacks limit the use of PDMS for wrinkle fabrication in consumer products due to its limited scalability and disadvantageous material properties. Therefore, an alternative material for wrinkle fabrication suitable with commercial manufacturing processes is proposed.

3.2 Wrinkle formation via heat-shrinkable thermoplastic films

Heat-shrinkable thermoplastic polymer films represent an attractive alternative as a platform for wrinkle formation because they are inexpensive, chemically inert, and

compatible with roll-to-roll manufacturing (thereby allowing for potential scale-up of fabricated technologies).[73]

We have previously demonstrated fabrication of micro- to nanoscale wrinkles using heat-shrinkable polymer films.[85] A thin layer of gold was deposited onto 2D blown PS film of PS. The substrate was shrunk by heating the PS at T = 160 ˚C (below the specified melting temperature of T = 240 ˚C). Biaxial retraction of the PS film (which has a stretch ratio of approximately 2.5) caused the stiff non-shrinkable gold layer to buckle and fold, thus creating multiscale wrinkles, as shown in **Figure 3.2**. Both uniaxial and biaxial wrinkles were formed by simply changing the boundary conditions. Control of wrinkle dimension was done by varying the thickness of the deposited gold skin layer from 10 to 50 nm. Using the heat-shrinkable PS, we created wrinkles with feature sizes down to 200 nm and 300 nm for the uniaxial and biaxial wrinkles, respectively. Even smaller structures with improved aspect ratio were fabricated using polyolefin (PO) shrink wrap film (which has a stretch ratio of approximately 4.3).[79] This polymer can shrink reproducibly 77% in length, allowing for formation of smaller features compared to those made on PS. The structures made using the shrink technology have been used for many applications such as cell and tissue engineering,[86–92] cell microarrays,[93–95] microfluidic components,[96–101] and surface sensing.[102–109]

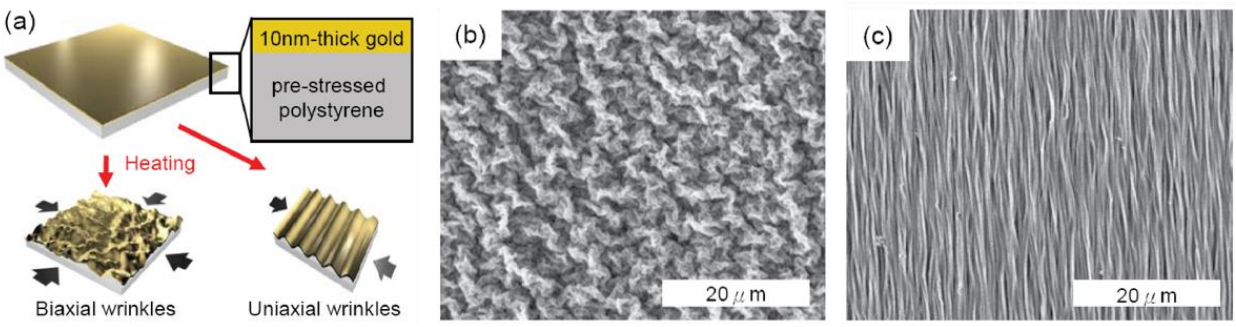

Figure 3.2. Micro- and nanofabrication on heat-shrinkable SMP film via surface wrinkling.[85] a) Scheme of fabrication of biaxial (left) and uniaxial (right) wrinkles on polystyrene sheets. SEM images of resulting b) biaxial and c) uniaxial wrinkles using gold. Adapted from C. C. Fu, A. Grimes, M. Long, C. G. L. Ferri, B. D. Rich, S. Ghosh, S. Ghosh, L. P. Lee, A. Gopinathan and M. Khine, *Adv Mater*, 2009, 21, 4472-+ with permission from John Wiley and Sons.

3.3 Formation of silica structures on the thermoplastic shrink wrap film

3.3.1 Silica structure fabrication

We leverage the stiffness mismatch between the thin SiO_2 layer and the PO film to create SiO_2 micro- and nanostructures. To fabricate the SiO_2 structures, SiO_2 was sputtered onto clean prestressed polyolefin (PO) film (a polyethylene and polypropylene copolymer) of thickness of 1 mil using ion-beam deposition system (MODEL IBS/e, South Bay Technology, Inc.) for a select period of time. 1 min of sputter deposition time was measured to deposit 1 nm of material. The coated film was then heated for 3 min at T = 145 ˚C. Heating the coated film past the melting temperature stated by the manufacturer (90-125 ˚C) causes the PO film to retract to 95% of its original area. Shrinkage of the stiff SiO_2 layer, which cannot shrink, instead buckles and folds, results in the formation of multi-scale SiO_2 structures. This process is illustrated in **Figure 3.3**.

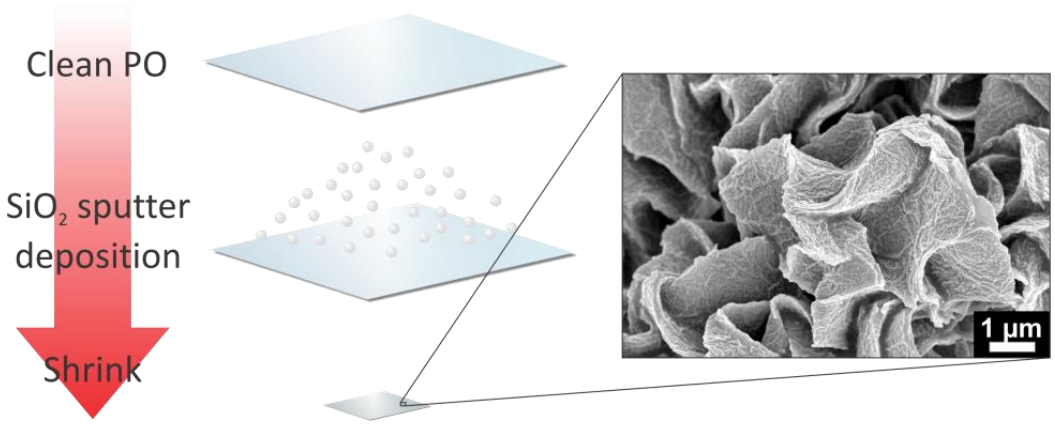

Figure 3.3. Schematic illustrating fabrication of the SiO_2 structures.

3.3.2 Characterization of silica structures

Deposition time of SiO_2 onto PO film was varied at 5 min, 10 min, 20 min, and 40 min and the deposition rate was measured to be 1 nm min^{-1} via an ellipsometer. 5 min, 10 min, 20 min, and 40 min of SiO_2 deposition was carried out on the clean PO film and top down Scanning Electron Microscopy (SEM) images of the resulting shrunk SiO_2 substrates (hereon referred to as PO-SiO_2) are shown in **Figure 3.4**. To prepare the substrates for top down SEM imaging, shrunk PO-SiO_2 substrates were sputter coated with 10 nm iridium (MODEL IBS/e, South Bay Technology, Inc.) and SEM images were obtained with 3.00 kV beam and 4 mm working distance (FEI Magellan 400 Scanning Electron Microscope). The 3D laser scanning confocal microscope (Keyence VK-X100K), which has a lateral resolution of 230 nm and z-axis resolution of 50 nm, was used to measure wrinkle height.

As expected, longer sputter deposition times resulted in features of bigger wavelength, as observed by the top down SEM images shown in **Figure 3.4**.[85] The cross sectional SEM images of the PO-SiO_2 substrates shown in **Figure 3.5** reveal that shrinkage of the PO-SiO_2 film results in the formation of hierarchical wrinkles ranging from the micron scale to nanoscale. Measurement of the higher generation wrinkles was done using the laser

scanning microscope at 100x (NA = 0.95, Nikon), and the resulting heights corresponding to the different thicknesses of deposited SiO_2 are shown in **Table 3.1**. We were also interested in the size distribution of the smaller nested nanoscale wrinkles. To determine the frequency distribution of the nanoscale SiO_2 wrinkles, two dimensional Fast Fourier transform (2D FFT) waveform analysis was performed using the upright SEM images using MATLAB. The results are shown in **Figure 3.6.** The probability distribution per individual substrate reveals a rather broad size distribution for the SiO_2 wrinkles on the substrate. However, the graph confirms a distinct red shift in the peak, from ~250 nm to ~500 nm as the deposited SiO_2 layer increased from 5 nm to 40 nm. This red shift can be explained by **Equation 4**, which describes wrinkle formation of bilayered films, where increased thin film thickness results in bigger wavelength sizes.

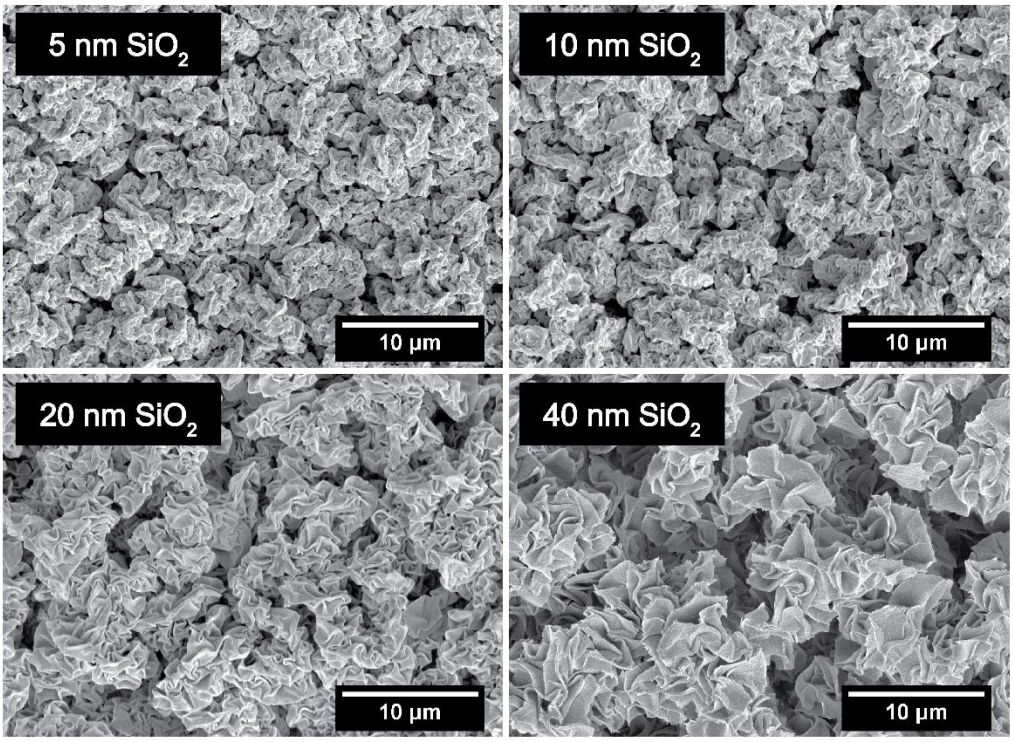

Figure 3.4. Top down SEM images of SiO_2 substrates generated on shrink wrap polymer film with different thicknesses of SiO_2.

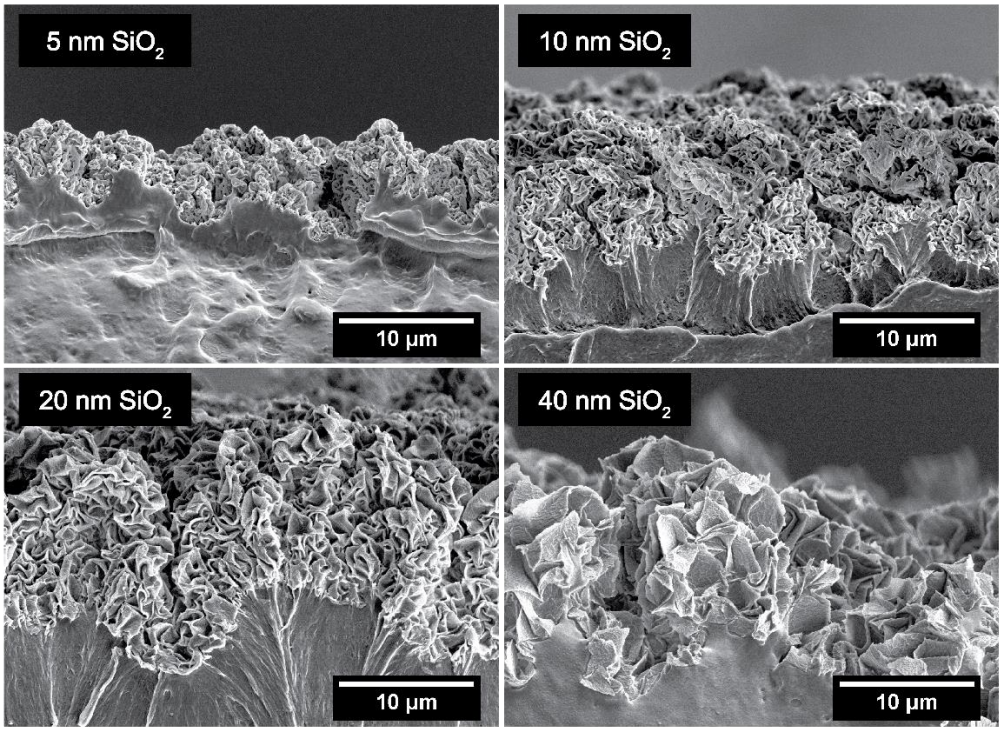

Figure 3.5. Cross-sectional SEM images of PO-SiO_2 substrates generated on shrink wrap polymer film with different thicknesses of SiO_2.

Table 3.1. Shrinking the SiO_2-coated PO polymer films results in substrates with different wrinkle heights.

Deposited SiO_2 Thickness (nm)	Shrunk Wrinkle Height (µm)
5	4.7 ± 0.2
10	6.4 ± 0.9
20	9.6 ± 1.3
40	10.6 ± 1.7

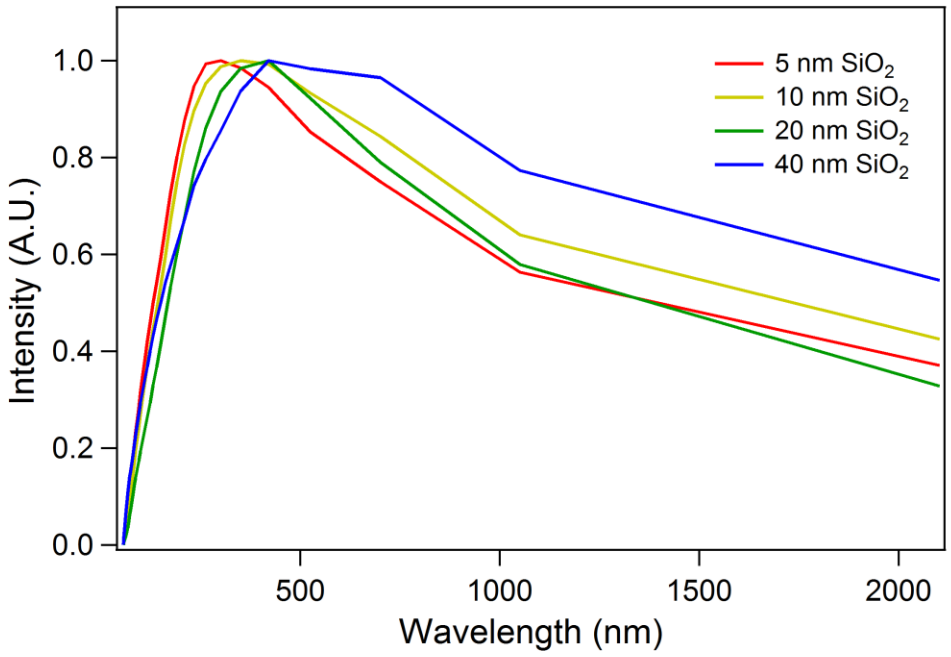

Figure 3.6. The FFT graph shows the probability distribution of the nested secondary SiO_2 wrinkles. Increased SiO_2 thickness causes a red shift in probability, as described by the wrinkling equation.

3.4 Summary

We leveraged the heat-retraction properties of the shrink film polymer to fabricate hierarchical SiO_2 structures. By changing thickness of the deposited SiO_2 layer, we were able to change the thickness (referred to as "height") and wavelength of the SiO_2 structures. The resulting structures following shrinkage of the bilayer films follow the wrinkling equation: thicker deposited films result in bigger wavelengths. This is confirmed through SEM images, laser scanning confocal analysis, and FFT analysis of the SiO_2 wrinkles. Following SiO_2 structure fabrication, we looked to apply the SiO_2 structures as a sensing platform.

CHAPTER 4: SURFACE FUNCTIONALIZATION

4.1 Biomolecule immobilization

4.1.1 Improvement upon prior work

As mentioned previously, we had demonstrated the ability to increase adsorbed immunoglobulin G (IgG) surface density using the PO film.[79] Briefly, PDMS stamps were oxygen plasma treated, dipped into rabbit IgG solution, and then incubated on the PO shrink film surface. The surface was blocked with 1% bovine serum albumin (BSA) to prevent nonspecific binding, then incubated with Alexa Fluor 555-conjugated anti-rabbit IgG to bind with the primary rabbit IgG, and then shrunk. The fluorescent intensity of the resulting shrunk microarray density was analyzed using fluorescence microscopy, and it was determined that a ~2-fold increase in the fluorescent intensity was observed from bringing the molecules closer in proximity. Since the flat polymer film is slightly hydrophobic, the proteins, when suspended within an aqueous solution, do not prefer to bind to the hydrophobic surface as the hydrophobic residues of the proteins are found within the core. This contributes to the low and inefficient surface adsorption. We theorized that by covalently linking the biomolecules, we obtain more specific and selective surface binding for sensing applications. Thus, we devised linking system to bind molecules onto SiO_2 substrates.

4.1.2 Biotin-streptavidin model linking system

The biotin-streptavidin complex has an association K_a of 10^{15} M^{-1}, being one of the strongest non-covalent linkages known in biochemistry.[110] The complex is composed of the protein streptavidin and a ligand biotin. Streptavidin is a tetrameric protein (66 kDa)

isolated from *Streptomyces avidinii* that contains four biotin binding sites. Streptavidin has a high thermostability with T_m = 73 ˚C, and it has been shown that upon biotin binding, the thermostability increases to T_m = 112 ˚C.[110] The biotin-streptavidin complex has been shown to be robust, withstanding extreme pH, denaturing agents, and enzymatic degradation.[111] Further making this affinity technology attractive is that biotin is a small molecule (244.31 Da). Its small size subsequently allows for conjugation to biologically active macromolecules without affecting their biological activity.[112]

Because of its tight binding capability and specificity, the biotin-streptavidin technology has been widely used and has found applications in biodetection,[113] cell imaging,[114,115] recombinant protein purification,[116–118] fluorophore tagging,[119] and protein immobilization.[120–123] Here, we use the biotin-streptavidin complex as a model linking system to immobilize protein for the initial protein binding studies. The substrate surface, either glass, PO film, and PO film sputtered with SiO_2 (PO-SiO_2), will be biotinylated and then reacted with streptavidin to represent protein binding to the surface.

4.2 Substrate preparation and biomolecule attachment

4.2.1 Surface silanization

Prior to linkage of biomolecules to the SiO_2 structures, cross-linking chemistry was verified on a glass slide. The glass surface was oxygen plasma treated (5 min). Introduction to atmospheric conditions after plasma treatment resulted in formation of hydroxyl groups on the plasma treated glass surface. The glass slide was then immersed in a solution of 2% v/v 3-aminopropyltrimethoxysilane (APTMS) for the attachment of reactive primary amines (**Figure 4.1a**). A change in contact angle (CA) was observed following silane treatment

(**Figure 4.1b**), which correlates with the presence of primary amine groups that render the glass surface slightly hydrophobic.[124,125]

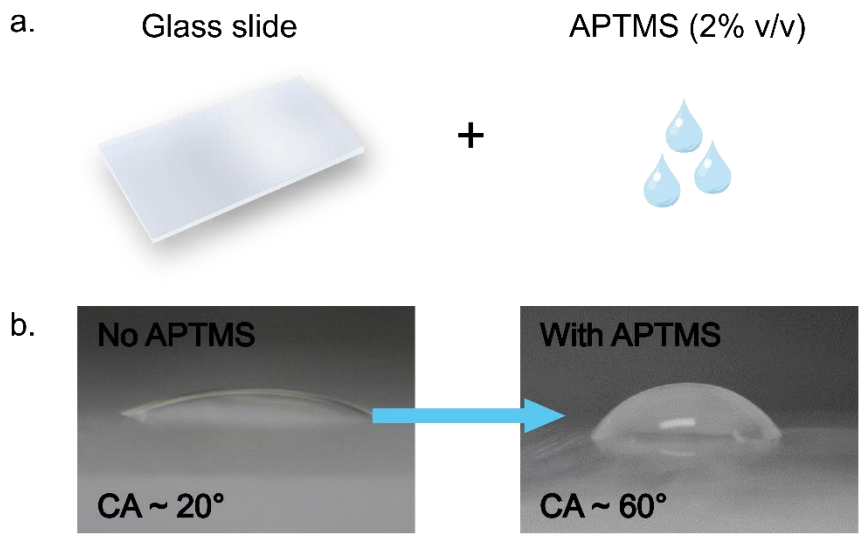

Figure 4.1. Schematic demonstrating the cross-linking chemistry done to chemically activate the surface using 2% v/v APTMS (a). The cross-linking chemistry was confirmed by measuring the CA of the treated surface. Addition of the primary amine groups change the glass CA from ~20 ˚ to ~60˚ (b).

The amine functionalized surfaces were biotinylated using EZ-Link Sulfo-NHS-LC-biotin (Piercenet ThermoScientific). For linkage studies, the Tetramethylrhodamine isothiocyanate (TRITC)-conjugated streptavidin (λ_{ex} = 550 nm, λ_{em} = 570 nm) served as the model protein of interest and was incubated on the biotinylated surface (50 min). Following incubation, the surface was washed and imaged on an upright epifluorescence microscope.

4.2.2 Optimization of model linking system

Optimization of biotin concentration was performed by ranging the concentration of EZ-Link Sulfo-NHS-LC-biotin. Concentrations of EZ-Link Sulfo-NHS-LC-biotin tested were 10 mg mL^{-1}, 1 mg mL^{-1}, 0.1 mg mL^{-1}, 10 µg mL^{-1}, and 1 µg mL^{-1}. 10 µg mL^{-1} of streptavidin-TRITC

(here on referred to as STRITC) was incubated on the surface, and the resulting fluorescence intensity per concentration of surface biotin was plotted as shown in **Figure 4.2**. Surface biotinylation was optimized to find a working concentration that would allow for maximal STRITC binding. It is also important to fine tune the amount of surface biotinylation as steric crowding has been shown to influence subsequent target binding.[5,123,126] By varying the EZ-Link Sulfo-NHS-LC-biotin concentration, we showed that the optimal concentration to maximize STRITC binding and minimize reagent volume use for the current set up to be 0.1 mg mL^{-1}.

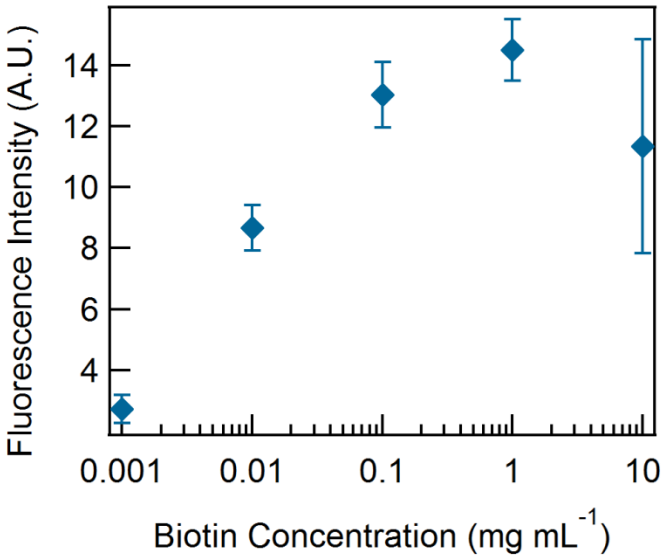

Figure 4.2. A logarithmic plot of the fluorescence intensity derived from bound STRITC per biotin concentration shows that the optimal concentration for surface biotinylation is 0.1 mg mL^{-1}.

4.2.3 Thermostability of model linking system

Because it is necessary to heat the PO-SiO_2 film past the PO melt transition temperature for the formation of SiO_2 structures, it was important to test if the biotin-streptavidin complex could withstand this temperature. To test the thermostability of the

biotin-streptavidin complex, the glass surface was first imaged using an upright epifluorescence microscope using a 2x objective (NA = 0.055, Edmond Optics) and then heated at T = 145 ˚C, the same temperature used to shrink the PO film. The surface was imaged again with the same settings and the signal following heating was compared to that before heating (**Figure 4.3**). 92 $\pm$ 0.02 % of the signal was maintained following heating, suggesting that the STRITC was still viable following heat treatment.

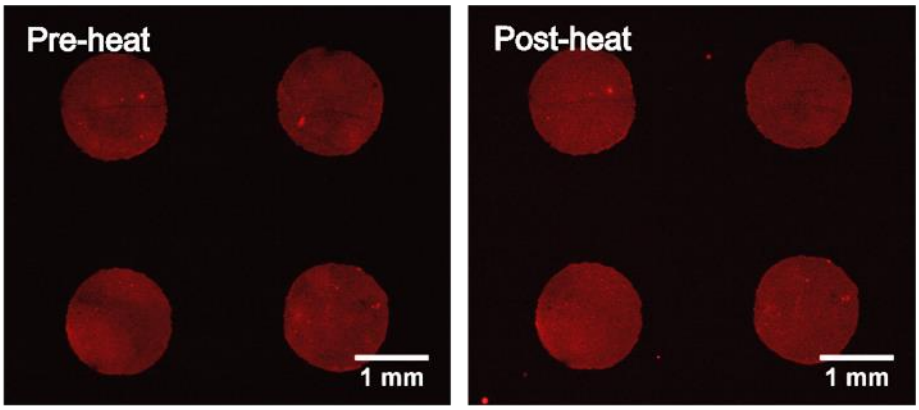

Figure 4.3. Fluorescent images of the STRITC bound glass surfaces pre- and post-heating at T = 145 ˚C. The fluorescent images are both artificially enhanced 98% for visibility.

4.3 Fluorescence signal enhancements

4.3.1 Binding on the silica structures

After establishing the binding conditions of STRITC to a glass surface, linkage of STRITC was then carried out on the SiO_2 coated PO film, which was then shrunk to create a functionalized PO-SiO_2 substrate. The fabrication procedure is outlined in **Figure 4.4**. First a shadow mask composed of a four-by-four array of circles with radii of 7.0 μm was designed using automated Computer-Aided-Design (AutoCAD) software and cut out of a sealing tape mask (Nunc™) with a VersaLASER cutter. The sealing tape mask was applied to the clean PO surface and then sputter coated with SiO_2. Here, we conduct the binding studies on 20 nm

SiO_2 surfaces. Binding studies on the flat PO-SiO_2 substrates were carried out with the same conditions as on glass. The PO-SiO_2 substrates were treated with oxygen plasma and immersed in an APTMS solution. The surface was biotinylated (0.1 mg mL^{-1}) and then spotted with STRITC (10 µg mL^{-1}). Following STRITC incubation, the surface was imaged on an upright epifluorescence microscope using a 2x objective (NA = 0.055, Edmond Optics). The functionalized PO-SiO_2 substrates (hence forth referred to as PO-SiO_2-STRITC) were shrunk at T = 145 ˚C to concentrate the molecules and induce structure formation. The shrunk surfaces were imaged again, and results were analyzed using ImageJ.

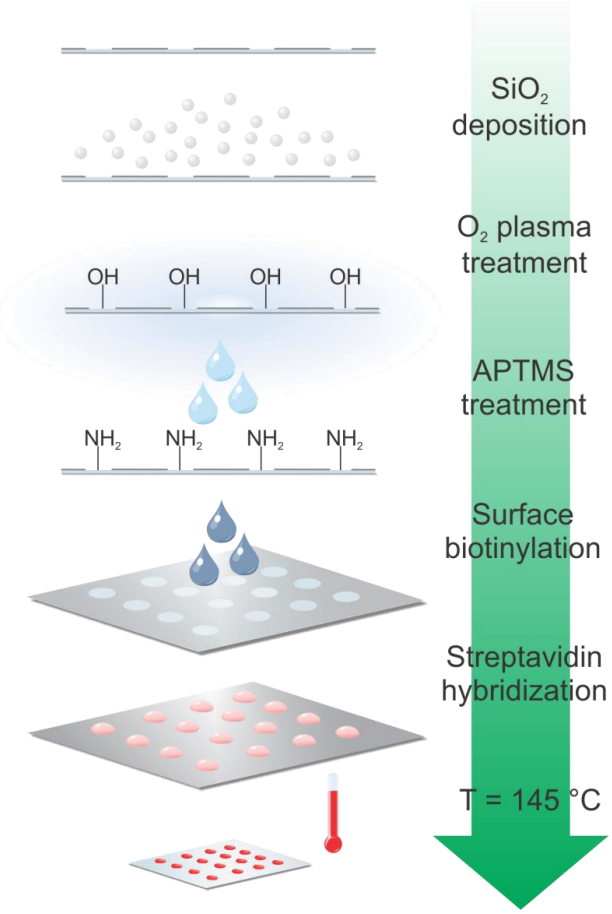

Figure 4.4. Schematic illustrating the fabrication of a shrunk PO-SiO_2-STRITC substrate. Clean PO is coated with a thin layer of SiO_2 through ion-beam sputter deposition, treated

with oxygen plasma, and reacted with APTMS for the attachment of reactive primary amines. The silanized surface was linked with biotin, reacted with STRITC, and shrunk.

The resulting fluorescent images and their respective 3D plot of their fluorescence intensities are shown in **Figure 4.5**. The change in fluorescence intensities of the shrunk PO-SiO_2-STRITC substrate was compared two ways: 1. To itself following shrinkage, referred to as the fluorescence signal increase (SI) and 2. With respect to the planar glass surface. The fluorescence SI **(Equation 5)** was calculated to be the fluorescence signal obtained after shrinking minus the background (here defined as the substrate without the presence of dye), over the fluorescence signal before shrinking minus the background:

$$Signal\ increase\ (SI) = \frac{Intensity_{postshrunk} - Intenstiy_{postshrunk,bg}}{Intensity_{preshrunk} - Intenstiy_{preshrunk,bg}} \qquad (5)$$

The enhancement over glass **(Equation 6)** was calculated to be the fluorescence intensity of substrate minus the background over the fluorescence intensity of the comparison substrate minus its respective backgrounds:

$$Enhancement\ over\ glass = \frac{Intensity_{exp,postshrunk} - Intensity_{exp,bg}}{Intensity_{glass,postshrunk} - Intensity_{glass,bg}} \qquad (6)$$

The fluorescence SI will first be addressed. As previously mentioned, the PO film experiences a 77% reduction lengthwise upon heating, which results in a theoretical 20-fold increase of surface area.[79] The PO-STRITC exhibited a fluorescence SI of 14-fold (standard error (SE) = 0.57) due to concentration of the surface bound fluorophores. This slight decrease in experimental value compared to the theoretical calculation was attributed to thermal degradation effects from heating. Interestingly, an approximate 50-fold (SE = 1.9)

fluorescence SI was observed on the shrunk PO-SiO_2-STRITC substrates, which drastically exceeds the calculated 20-fold increase. (This effect will be discussed in the optical characterization section.) Notably, the fluorescence SI was accompanied with a significantly increased SNR (defined as the ratio of the raw fluorescence signal to the background signal) from 11:1 to 76:1. The SI obtained from shrinking the PO-SiO_2-STRITC substrate exceeded that observed from just concentrating the fluorescent molecules (as seen on the PO-STRITC substrate). This suggests that the additional increase of fluorescence signal on the shrunk PO-SiO_2-STRITC substrate is due to presence of SiO_2 structures and not from bringing the fluorophores into close proximity of each other. It was also shown on the glass surface that the application of heat did not cause signal amplification or significant signal degradation (SI_{glass} = 0.92, SE = 0.019) and that the SNR did not change considerably (from 5.7:1 to 5.2:1 following heating). From this, we conclude that the difference in fluorescence SI on the shrunk PO-STRITC and the shrunk PO-SiO_2-STRITC is not due to thermal effects on the fluorophore, and that the SiO_2 structures are an important contributing factor in creating these significant fluorescence signal enhancements.

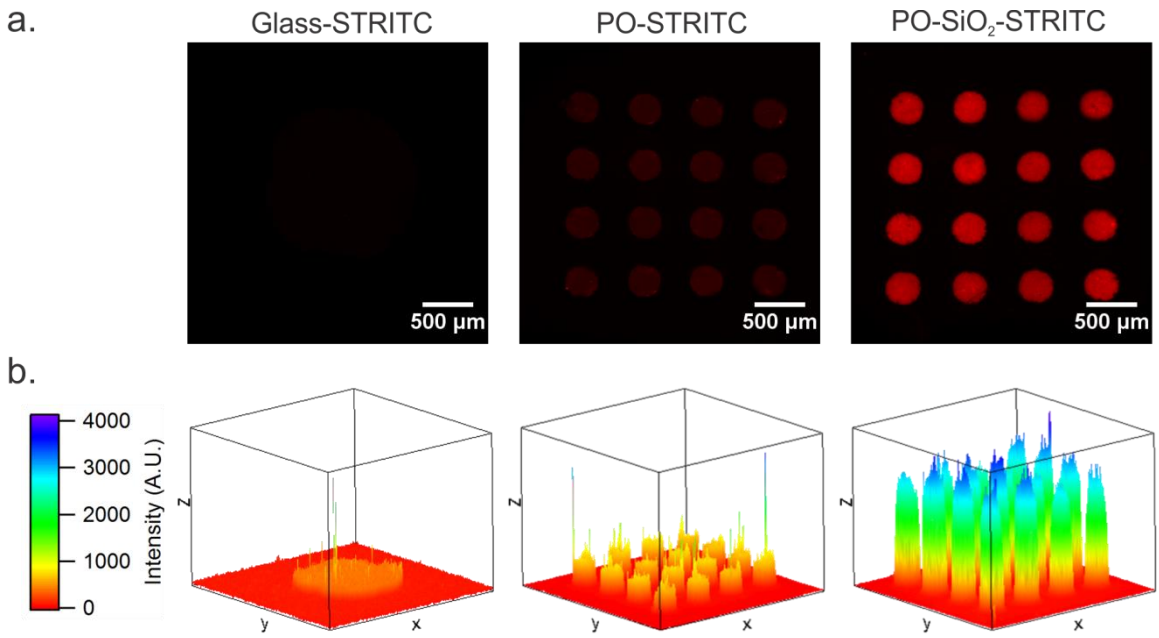

Figure 4.5. Fluorescent images of patterned surfaces for heated glass, thermally shrunk PO, and thermally shrunk PO-SiO_2 bound with biotin and STRITC (a) and the corresponding 3D fluorescence intensity profiles (b).

Next, a comparison to a planar glass surface was done. The shrunk PO-STRITC had an enhancement value over glass of 25 (SE = 3.1). The shrunk PO-SiO_2-STRITC substrate had an enhancement over glass value of 116 (SE = 9.7). A higher fluorescence signal was observed on the flat PO-SiO_2-STRITC relative to glass-STRITC; we attribute this increased fluorescence signal to the inherent reflectivity of the PO film (as shown later in Chapter 5).

4.3.2 Wavelength independent fluorescence signal enhancements

While fluorescence enhancements that arise from plasmon resonances are highly dependent on nanostructure size and shape,[127] we show that increased fluorescence signal and fluorescence enhancement factors on our PO-SiO_2 substrates are not restricted to a particular wavelength or structure size. 10 µgmL^{-1} Cy2-conjugated streptavidin (λ_{ex} = 492

nm, λ_{em} = 510 nm) were spotted onto unshrunk biotinylated substrates as previously performed. Upon shrinking the substrate, a 39-fold (SE = 1.6) and 11-fold (SE = 1.2) increase in the fluorescence signal is observed on the shrunk PO-SiO_2 substrate and the shrunk PO substrate, respectively. The increases in fluorescence signal correspond to averaged enhancement factors of 106 (SE = 9.5) and 5.0 (SE = 0.27) for the shrunk PO-SiO_2 relative to the heated glass and shrunk PO substrate. An increase in SNR is also experienced on the shrunk PO-SiO_2 substrate from 13:1 to 29:1.

4.4 Summary

We used a model-linking system to covalently link fluorescently labelled protein onto the surface of the SiO_2 structures. We optimized the concentration of the EZ-Link Sulfo-NHS-LC-biotin and verified that the biotin-streptavidin model linking system was able to withstand the thermal conditions associated PO film shrinkage. Biotin was crosslinked to the surface of the substrates (glass, PO, and PO-SiO_2), and a fluorescently conjugated STRITC served as the target protein of interest. We showed that by heating the conjugated PO-SiO_2 film, thus creating the SiO_2 structures, we were able to achieve robust, far-field fluorescence signal enhancements that exceeds those expected from merely concentrating the molecules on the surface. Fluorescence SI of the shrunk, labelled PO-SiO_2 relative to planar glass was ~116-fold and the Enhancement over Glass of the labelled PO-SiO_2 was ~50-fold. Furthermore, the enhancements are not wavelength dependent, and was also observed using an alternate protein of interest Cy2-conjugated streptavidin. Here, proof-of-concept was demonstrated using 20 nm SiO_2 sputtered polymer films. Next we look to characterize

the optical properties and identify the mechanism(s) responsible for the fluorescence signal enhancements on the SiO_2 structures.

CHAPTER 5: OPTICAL CHARACTERIZATION

5.1 Optical properties of the functionalized surfaces

To understand the effects of the SiO_2 structures on the fluorescently labelled streptavidin, the optical properties of the fluorescently conjugated substrates were examined by measuring the absorbance spectrum and emission spectrum of the conjugated surfaces. 20 nm thick SiO_2 coated PO films were prepared and conjugated with STRITC using the methods described in Chapter 4. The functionalized substrates were shrink and UV-visible absorption spectra were collected using a PerkinElmer Lambda 950 UV/Vis/NIR Spectrophotometer with a 60 mm integrating sphere detector. Fluorescence spectra were measured with an excitation wavelength of 561 nm and emission was collected from 416 – 728 nm (Zeiss LSM 710) using a 20x objective (NA = 0.4, Zeiss Korr C-Apochromat) and an argon laser.

The absorbance and emission spectra measured are shown in **Figure 5.1.** Optical properties are important indicators of how the molecule of interest is interacting with its environment. **Figure 5.1a** is the UV-Vis absorption spectra of STRITC, glass-STRITC (STRITC bound to glass) and shrunk PO-SiO_2-STRITC. STRITC exhibited two absorption maxima at 520 and 549 nm which were attributed to the presence of dimeric and monomeric species. The presence of dimeric and monomeric species was reported to occur for rhodamine dyes at high concentrations ($A_{520/549}$ = 0.89).[128] Glass-STRITC also exhibited an absorption maximum at 549 nm. Covalent linkage of STRITC within the SiO_2 structures was not observed to cause spectral shifts in peak absorbance. The absorption spectra of the shrunk PO-SiO_2-STRITC substrate shows higher optical density at higher energies, which fits well to Rayleigh

scattering, suggesting that shrinking of the PO-SiO_2 substrate creates rough 3 structures that result in light scattering.[129]

The emission spectra are shown in **Figure 5.1b**. The emission intensity maximum for the STRITC occurred at 575 nm. While covalent attachment of the STRITC on glass did not cause a change in the absorption wavelength, it was observed to cause a slight red shift of 3 nm for the emission wavelength for STRITC on the PO-SiO_2 substrate. This slight red shift in emission wavelength could be attributed to the change in molecular surrounding of the STRITC dye since it is known that dye molecules are affected by microenvironment polarity.[12] However, the observed spectral shifts were insignificant and it could be suggested that confinement of the dye molecules within the SiO_2 structures does not result in significant changes of the dye's electronic structure.

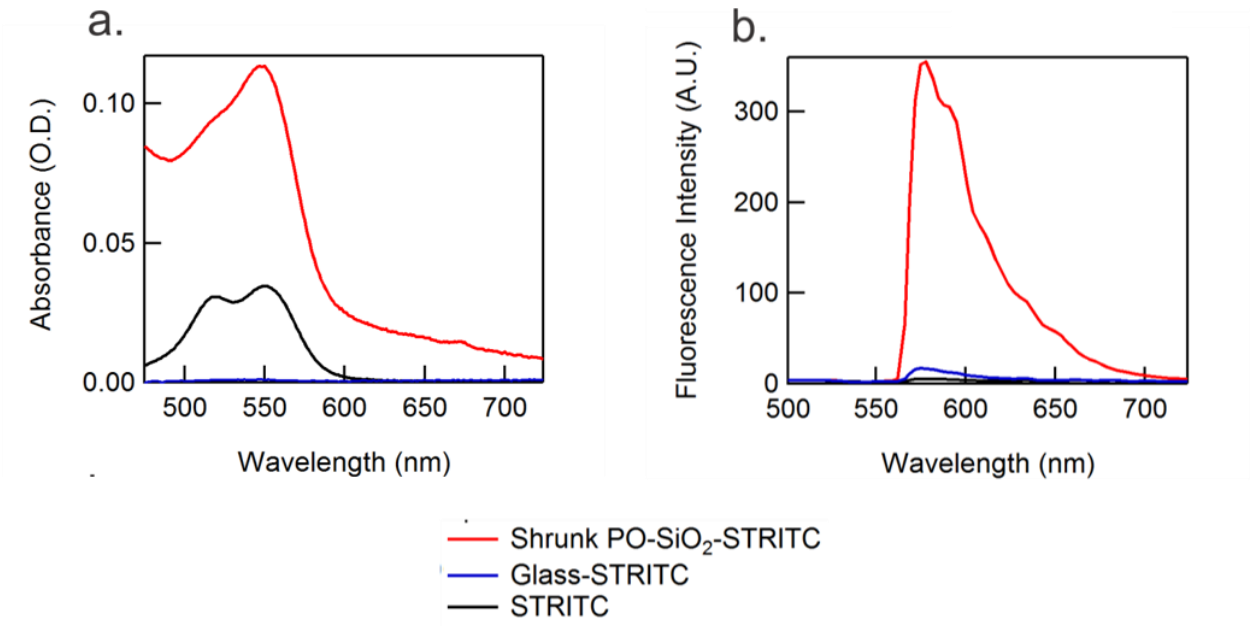

Figure 5.1. Absorption spectra of STRITC free dye, glass-STRITC, and PO-SiO_2-STRITC (a) and emission spectra of STRITC free dye, glass-STRITC, and PO-SiO_2-STRITC (b).

The spectroscopic studies done on the functionalized substrates confirmed biomolecule conjugation and verified the concentration effect as evidenced by higher signals

on the shrunk SiO_2 structures. However, because there were no significant spectral shifts were observed in the spectra, further studies are necessary to characterize the mechanism behind the fluorescence signal enhancements.

5.2 Integrating sphere measurements

The scattering properties of the SiO_2 structures were first explored through integrating sphere measurements. The integrating sphere quantifies the transmittance and reflectance of highly scattering surfaces. Clean PO films were sputtered with different thicknesses of SiO_2 (0, 5, 10, 20, 40 nm). The SiO_2-sputtered films were shrunk to create the multiscale SiO_2 structures. The transmittance and reflectance spectra of the SiO_2 structures were collected from 800 – 400 nm using the PerkinElmer Lambda 95 UV/Vis/NIR Spectrophotometer with a 60 mm integrating sphere detector. The plotted spectra are shown in **Figure 5.2** and **Figure 5.3**.

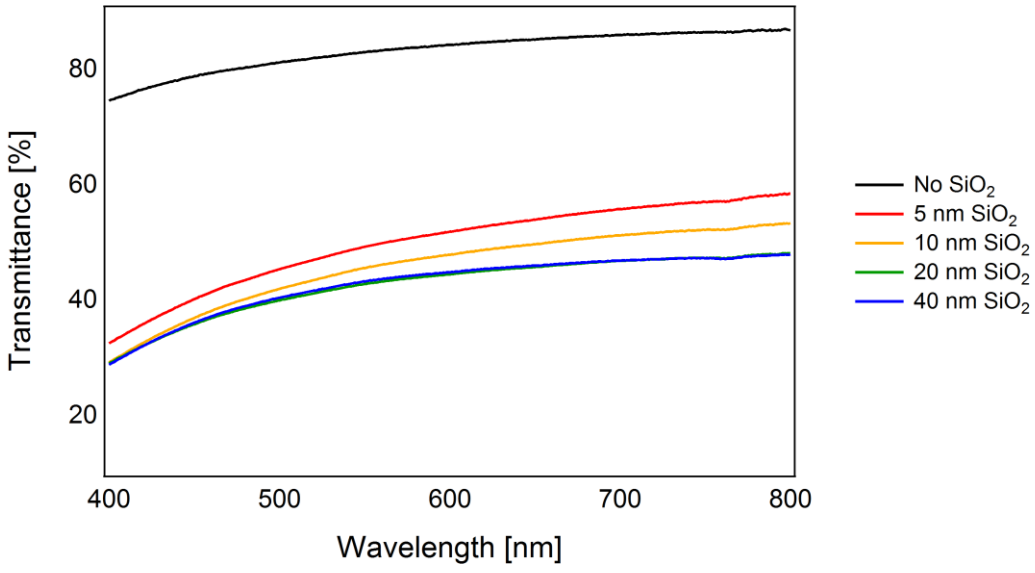

Figure 5.2 A graph of the percent transmittance of surfaces with different thicknesses of deposited SiO_2 across the visible wavelengths. Increased thickness of SiO_2 results in reduced transmittance of the substrates across the visible wavelengths.

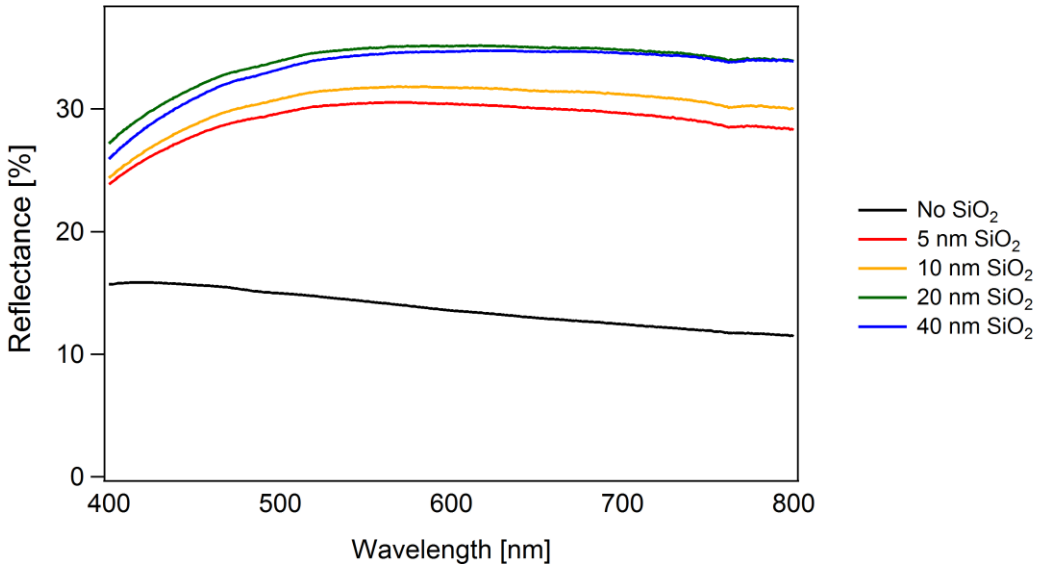

Figure 5.3 A graph of the percent reflectance of surfaces with different thicknesses of deposited SiO_2 across the visible wavelengths. Increased thickness of SiO_2 results in increased reflectivity across the visible wavelengths.

In **Figure 5.2**, the transmittance spectra of the SiO_2 substrates reveals that as the thickness of the deposited SiO_2 layer increases, the measured percent transmittance of the substrate decreases, as expected. The shrunk PO films (20 nm SiO_2 and 40 nm SiO_2) have similar transmittance spectra and overlap in the graph. **Figure 5.3** is a graph of the measured percent reflectance of each substrate. The graph reveals that the PO film is inherently reflective, which explains the increased fluorescence signal read on the flat, unshrunk fluorescently-conjugated PO film relative to the glass control. Furthermore, as the deposited thickness of SiO_2 increases from 5 nm to 40 nm, the shrunk substrate exhibits higher percent reflectance. The increased reflectance upon the addition of the SiO_2 structures indicates that the SiO_2 structures make up a highly scattering surface. Interestingly, the measured percent reflectance and transmittance of the 20 nm and 40 nm deposited SiO_2 samples are similar, while incremental changes are observed from 0 nm to 20 nm deposited SiO_2 substrates.

5.3 Confocal pinhole experiment

5.3.1 Confocal microscopy

We devised an experiment that capitalizes on the confocal microscope's ability to reject out-of-focus light in order to characterize the scattering nature of the SiO_2 structures. The differences between a wide-field epifluorescence microscope and a confocal microscope are briefly discussed as follows.

A schematic of an upright epifluorescence wide-field fluorescence microscope is shown in **Figure 5.4**. The fluorescence source produces a bright white light that is passed through an excitation filter. The excitation light is directed to the sample through a dichroic mirror and illuminates the entire sample. The emitted light from the sample is redirected through the dichroic mirror, through the emission filter and into the detector. The wide-field epifluorescence microscope collects all the light that is emitted and reflected back from the sample. This property limits the effectiveness of wide-field microscopy when imaging samples that have finer structures (smaller than the diffraction limit at about 200 – 300 nm) or increased thickness (greater than 2 μm) as collection of all the emitted light can lower image resolution.

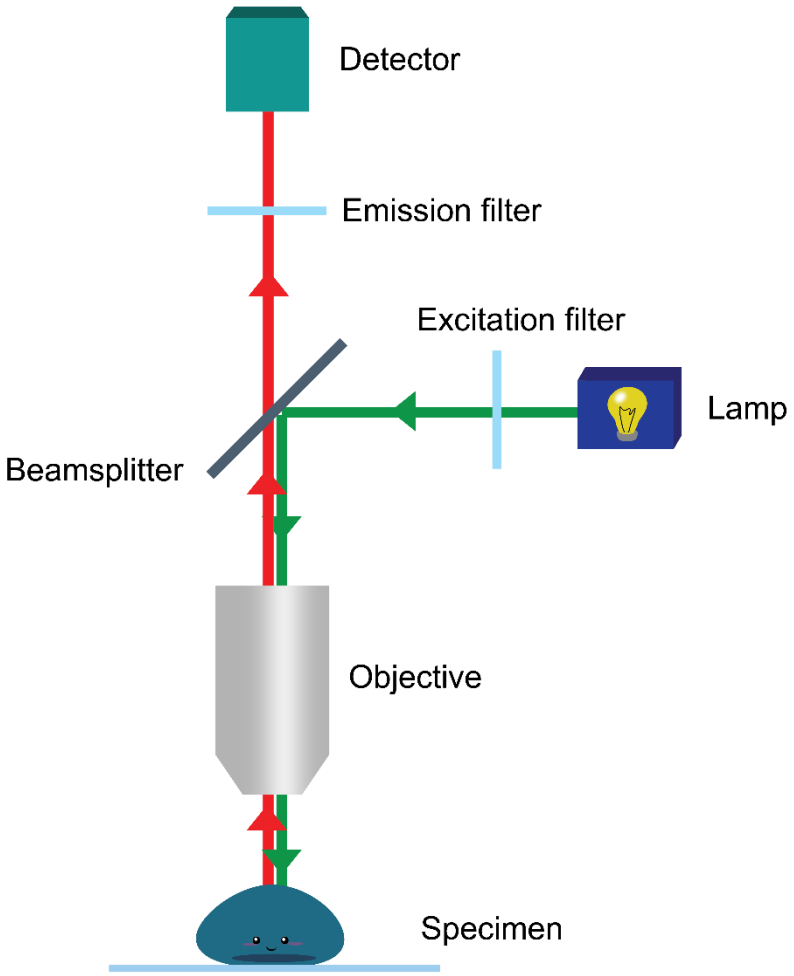

Figure 5.4. A schematic illustrating the workings of a widefield fluorescence microscope.

Confocal microscopy addresses this problem of lowered image resolution with the addition of pinholes, which suppresses out-of-focus light from above or below the focal plane. This produces images with increased optical resolution and allows for optical sectioning and therefore 3D reconstruction of images. A simplified schematic of confocal microscopy is shown in **Figure 5.5**. Briefly, a high excitation laser is used to excite the sample. The laser passes through the excitation pinhole, which limits the illumination of the sample to a small region in the focal plane. After sample illumination (thereby excitation), the emitted light coming from the sample passes through the dichroic mirror and through

the emission pinhole, which restricts the light reaching the detector to that from the focal plane. A raster scan of the sample is done to create a composite image with the desired field of view.

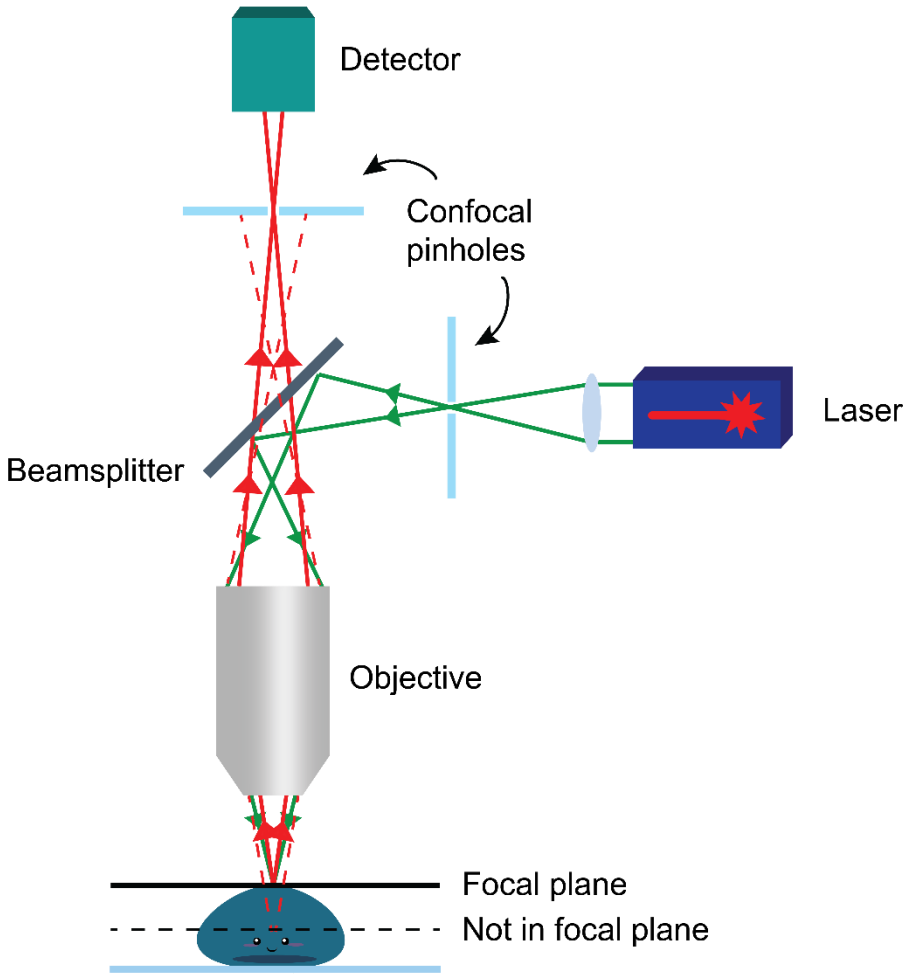

Figure 5.5. A simplified schematic illustrating the workings of a confocal microscope.

5.3.2 Pinhole scanning experiment

We leverage the ability of a confocal microscope to suppress out-of-focus signals to investigate the scattering properties of the SiO_2 surfaces. We performed the scanning pinhole experiments, which involved using the confocal microscope to repeatedly excite and collect

the emission from the sample while moving the emission pinhole location. The pinhole scanning experiment of the bio-functionalized SiO_2 substrates was performed using laser confocal microscopy (Olympus FV1000) at the Laboratory for Fluorescence Dynamics (University of California, Irvine). The substrates were prepared by first functionalizing the SiO_2-coated films (0, 5, 10, 20, 40 nm) with streptavidin-TRITC using the same conditions as previously described. The surfaces were thermally shrunk to create fluorescently labelled SiO_2 structures. The substrates were excited at 559 nm and emission was collected at 575 – 620 nm using a 20x objective (NA = 0.75) with 488 nm light. The emission of the fluorescently labelled substrates was collected as the pinhole was displaced in the x-axis in 100 μm steps. Fluorescence images with the pinhole open were taken using a 10x objective (NA = 0.40). Images were analyzed using ImageJ.

In this study, we repeatedly imaged the same region with different pinhole positions. By misaligning the detection pinhole, which exists to eliminate out-of-focus light, we expect to see significantly reduced fluorescence signal as the focal volume gets further away from the detector. The results from this experiment are plotted in **Figure 5.6**, which is a graph of the normalized fluorescence intensity as a function of the pinhole misalignment. As expected, there is a drop in the collected emission as the detection pinhole becomes more misaligned for all substrates (0, 5, 10, 20, 40 nm SiO_2). More interestingly, **Figure 5.6** reveals that as we increase the SiO_2 thickness from 5 nm to 40 nm, a higher fluorescence emission is collected at each respective pinhole misalignment. The fluorescence decay due to pinhole misalignment slows down as the SiO_2 thickness increases until the SiO_2 thickness of 20 nm is reached. The collected fluorescence emission from the 40 nm deposited SiO_2 follows the same decay rate observed on the 20 nm substrates, suggesting a limit to the size or thickness

effect on the emitted fluorescence intensity. Overall, more fluorescence emission on substrates with SiO_2 structures was collected through a misaligned detection pinhole. This suggests to us that the SiO_2 structures represent a highly scattering surface that scatters the emitted fluorescence out of the focal volume that is detected when the pinhole is misaligned.

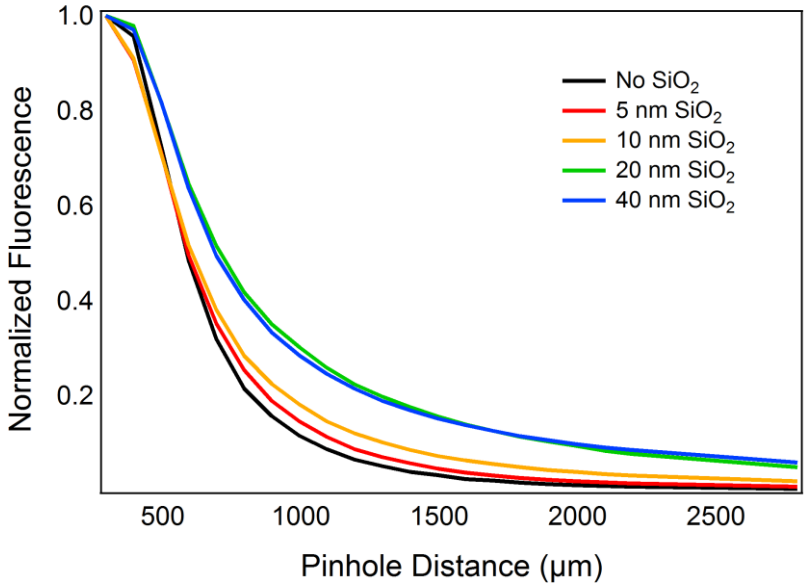

Figure 5.6. Graphical illustration of the normalized fluorescence as a function of pinhole misalignment on substrates with different thicknesses of SiO_2. At each increased SiO_2 thickness (5 nm to 40 nm), a higher fluorescence emission is collected at each respective pinhole misalignment.

5.3.3 Confocal z-stacks

As previously mentioned, one of the advantages of confocal microscopy is its ability to suppress out-of-focus light and isolate signals from a single focal plane. This allows for 3D reconstruction of the sample with high resolution. We compared the total fluorescence on the functionalized SiO_2 surfaces quantified with confocal z-stacks to that obtained using an upright epifluorescence microscope in order to isolate the fluorescence signal arising from a single focal plane. To do so, STRITC was linked onto the flat PO-SiO_2 films (0, 5, 10, 20, 40 nm) using the previously described conjugation methods. The substrates were shrunk and

imaged using laser confocal microscopy (Olympus FV1000) at the Laboratory for Fluorescence Dynamics (University of California, Irvine). The surfaces were thermally shrunk to create fluorescently labelled SiO_2 structures. Confocal z-stacks (scan range 50 μm, 1 μm steps) of the fluorescently labelled substrates were acquired by exciting the substrates at 559 nm and collecting the emission from 575 – 620 nm using a 20x objective (NA = 0.75) with 488 nm light.

Taking z-stacks allows us to eliminate light from outside the focal plane and quantify the fluorescence from individual z-slices. A 3D reconstruction of the functionalized SiO_2 substrates would only detect fluorescence from a single focal plane and eliminate all scattered light. The results from the confocal z-stack experiment are shown in **Figure 5.7a**, which is a graph of the fluorescence intensity of the functionalized surface as a function of distance throughout the substrate in the z-axis. Both fluorescently conjugated SiO_2 structures and shrunk PO film show similar trends throughout the sample, the integrated intensity reveals that the two substrates have very similar total intensity, where the integrated fluorescence intensity is about $(4 \pm 0.5) \times 10^3$ AU and $(4 \pm 0.2) \times 10^3$ AU on the SiO_2 structures and shrunk PO film, respectively. We opened the pinhole to collect all the emitted light, which includes scattered out-of-plane light. The fluorescence images are shown in **Figure 5.7b**, where the observed fluorescence on the SiO_2 structures (left) is greater than that on the shrunk PO film (right). The fluorescence intensity on the SiO_2 structures measured ~2.6-fold greater than that obtained on the shrunk PO film. This discrepancy between the fluorescence intensity measured from the integrated z-stacks and that measured from the wide-field image validates that out-of-focus light contributes to the enhanced fluorescence SI.

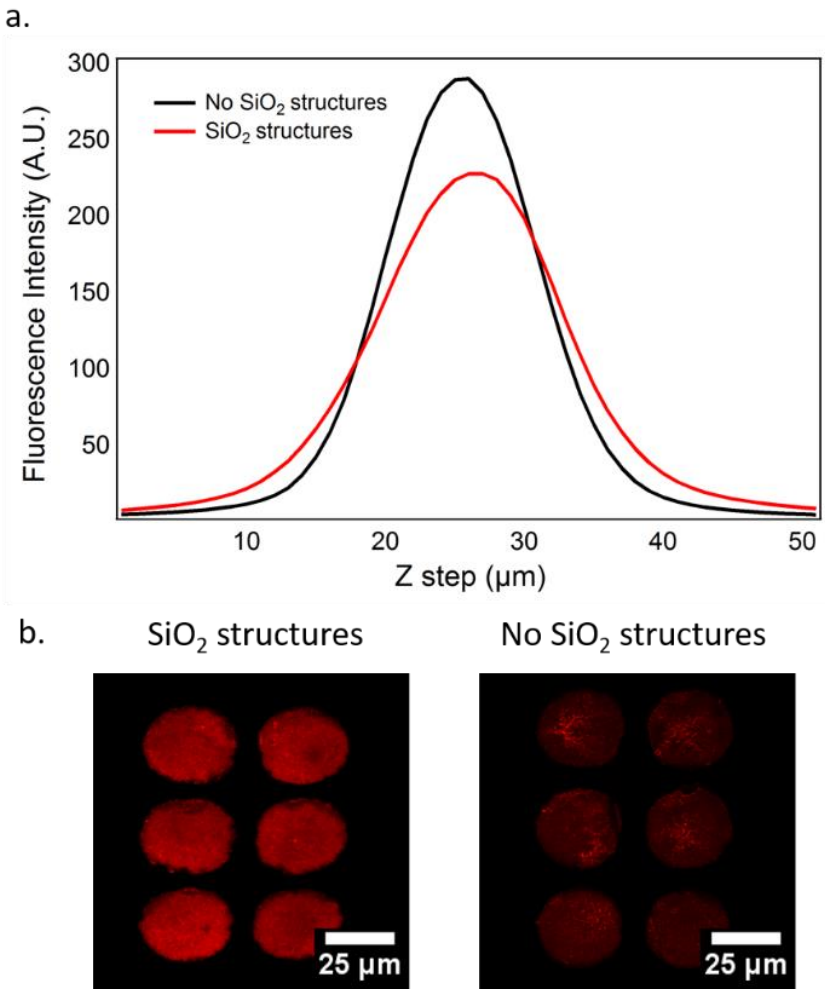

Figure 5.7. Fluorescence imaging to characterize scattering effects of the SiO_2 structures. A confocal z-stack of fluorescently labelled substrates shows that the overall trend of fluorescence intensity across the z-axis is very similar between substrates with SiO_2 structures and without the SiO_2 structures (a). Integrated intensity across the substrate yields very similar total fluorescence intensity. Fluorescence images of the same substrate taken with an open confocal pinhole show that the substrates with SiO_2 structures have greater fluorescence intensity compared to the shrunk polymer film without SiO_2 structures (b).

5.4 Theoretical approximation of enhancement based off scattering effects

The optical characterization studies indicated that the SiO_2 structures are highly scattering. We observed with increased SiO_2 deposition thickness, larger scattering effects

are observed. We looked to approximate a theoretical scattering enhancement factor (SEF). We attribute the enhancement to a combination of both scattered excitation light and scattered emission light. This approximation is broken down **Equation 6:**

$$\text{SEF} = \left(\frac{\%R,n\ nm_{\lambda,ex}}{\%R,0\ nm_{\lambda,ex}}\right) + \left(\frac{\%R,n\ nm_{\lambda,em}}{\%R,0\ nm_{\lambda,em}}\right) * \left(\frac{collection\ solid\ angle}{2\pi}\right) \quad (6)$$

where the $\%R,n\ nm_{\lambda,ex}$ is the percent reflectance of the substrate with n thickness of deposited SiO_2 at the dye's excitation wavelength, $\%R,0\ nm_{\lambda,ex}$ is the percent reflectance of the substrate with no SiO_2 structures at the dye's excitation wavelength, $\%R,n\ nm_{\lambda,em}$ is the percent reflectance of the substrate with n thickness of deposited SiO_2 at the dye's emission wavelength, $\%R,0\ nm_{\lambda,em}$ is the percent reflectance of the substrate with no SiO_2 structures at the dye's emission wavelength, The collection solid angle is a factor that accounts for the amount of light detectable with the microscope objective. The theoretical SEF for each substrate at different thicknesses of SiO_2 is calculated based on the reflectance data obtained from the integrating sphere measurements and tabulated in **Table 5.1**.

We looked to verify the theoretical approximations for the SEF. The effects of the SiO_2 deposited layer on the resulting fluorescence enhancements are explored. SiO_2-coated films (0, 5, 10, 20, 40 nm) were functionalized with STRITC using the previously described conditions, imaged at 2x (NA = 0.055, Edmund Optics) using an upright epifluorescence microscope, thermally shrunk, and imaged again.

We observe increased fluorescence intensity on the shrunk surfaces with increased deposited SiO_2 as seen in **Figure 5.8**. The SEF observed on the shrunk substrates with different SiO_2 structures are calculated from the fluorescence intensities and shown in **Table 5.1.** As we increase the deposited thin film thickness from 5 nm to 40 nm, the experimental

SEF increases until it plateaus at 20 nm of deposited SiO_2. This trend follows that followed by the theoretical SEF. The discrepancy at lower thicknesses of deposited SiO_2, such as at 5 nm of deposited SiO_2, can be attributed to discontinuities of the deposited thin film at that thin of a layer.

The experimental SEF of the substrates at different thicknesses of deposited SiO_2 complements the results obtained with the integrating sphere measurements, where incremental increases in reflectance spectra are observed as the SiO_2 layer is increased until the differences become negligible at 20 nm of deposited SiO_2. This trend is also observed in the pinhole scanning experiment, where increased SiO_2 thickness yielded higher scattering effects, with the maximal scattering achieved at 20 nm deposited SiO_2.

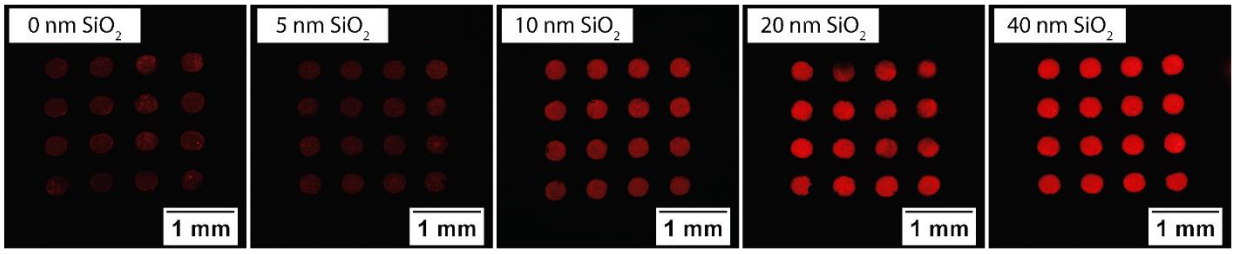

Figure 5.8. Fluorescent intensity images of the resulting shrunk PO-SiO_2 surfaces at different deposited thickness of SiO_2.

Table 5.1. Increasing the thicknesses of deposited SiO_2 results in higher enhancement factors based on the scattering effects

Deposited SiO_2 Thickness (nm)	Theoretical SEF	Experimental SEF
0	---	---
5	2.1	1.0 ± 0.1
10	2.2	1.8 ± 0.2
20	2.4	2.3 ± 0.4
40	2.4	2.5 ± 0.5

The optical scattering dependence on the deposited SiO_2 thickness can be explained through the wavelength equation, as shown in **Equation 4**, where λ is the resulting wrinkle wavelength, *h* is the thickness of the film skin layer, ν_f and ν_s represent the Poisson's ratio of the thin film and the Poisson's ratio of the substrate, respectively. E_f and E_s are the elastic modulus of the film skin layer and substrate, respectively.[80,85]

$$\lambda = 2\,\pi\,h\left[\frac{\left(1-\nu_f^2\right)E_s}{3\left(1-\nu_s^2\right)E_f}\right]^{1/3} \qquad (4)$$

We assume the Poisson's ratios and elastic moduli to be constants for the substrate and polymer film to be constants. **Equation 4** shows us that as the deposited SiO_2 film thickness increases from *h* = 5 to 40 nm, larger feature sizes should be obtained on the shrunk polymer substrates. This was confirmed through the SEM images of the shrunk SiO_2 substrates in **Figure 3.4,** and **3.5 (Chapter 3)**. **Table 3.1 (Chapter 3)** also revealed the SiO_2 wrinkle amplitudes upon shrinkage of the sputtered films plateaus at 20 nm of deposited SiO_2. The increased depth, or amplitude, associated with the shrunk 20 nm and 40 nm PO-SiO_2 substrate offer more surface area available to scatter light, and the multiple scattering effects that occur produce diffuse light that increases the absorption / excitation and subsequently emission rate of attached fluorophores.

5.5 Summary

Initial spectroscopic studies of the shrunk functionalized 20 nm SiO_2 surfaces indicated that the SiO_2 structures may exhibit scattering capabilities. In this chapter, we

aimed to further characterize the optical properties of the SiO_2 structures. Transmittance and reflectance spectra were obtained using an integrating sphere. As expected, the light transmitted through the shrunk substrates across the visible wavelengths decreased as the thickness of the sputtered SiO_2 layer increased. The reflectivity of the shrunk substrates increased as the thickness of the deposited SiO_2 layer is increased. This suggested that the larger SiO_2 wrinkles scatter more light. Furthermore, the incremental decreases in transmittance and increases in reflectance were observed as the SiO_2 thickness was increased from 0 nm to 10 nm, however the differences were negligible between the 20 nm and 40 nm thick SiO_2 substrates. The dramatic increase in reflectance that occurred due to the presence of the SiO_2 structures suggested the SiO_2 structures are highly scattering. This was confirmed through additional experiments. We showed with the pinhole scanning experiment that increased thicknesses of SiO_2 resulted in more light detected as a function of pinhole misalignment. The increased fluorescence signal per pinhole misalignment suggested the SiO_2 wrinkles scatter light out of the focal volume, and that a relationship between SiO_2 thickness and degree of scattering exists. Confocal z-stacks of the functionalized substrates were collected to further verify that the enhanced fluorescence signal is attributed to out-of-focus light. We showed the total fluorescence intensity integrated over the entire sample on the substrates with and without the presence of SiO_2 structure yielded similar fluorescence intensities. When the confocal pinholes were opened entirely, illuminating the entire functionalized substrate, the fluorescence intensities between the substrate with and without SiO_2 structures was $\sim$ 2.5-fold. The difference in fluorescence intensities that arose merely from using the confocal pinhole pointed to out-of-

plane scattering as a major contribution to the enhanced fluorescence signals observed on the SiO_2 structures.

Using the results obtained from the optical characterization studies, we derived an approximation for the fluorescence enhancements based on scattering effects alone. This approximation, which we called the SEF was calculated and verified with experimental data, which we obtained when we looked at the changes in fluorescence intensities on bio-conjugated substrates with different thickness of SiO_2 upon shrinkage. An increase in the fluorescence SEF was observed upon an increase in deposited SiO_2 thickness. The relationship between the fluorescence SEF and the increased SiO_2 thicknesses was explained through the increased surface area that was produced upon the addition of the SiO_2 layer. Thicker films have bigger amplitudes, therefore greater surface area becomes available for light scattering. More scattered excitation light results in greater probability for emitted light.

CHAPTER 6: APPLICATIONS IN DISEASE DIAGNOSTICS

6.1 Disease detection

The driving motivation behind this work is to develop POC applicable technologies to address the unmet need of inexpensive and effective diagnostic tools. Early detection of diseases enable early diagnosis, and therefore treatment and containment. As previously mentioned, surfaces for enhanced fluorescence detection typically involve complicated fabrication techniques with multiple steps and use expensive materials such as gold or silver. These factors impede translation of these effective substrates towards POC applications. Here, we demonstrated the ability to fabricate fluorescence enhancing SiO_2 structures merely through heating shrink wrap polymer film. The method is rapid, uses inexpensive materials, and signals are detected using a simple fluorescence microscope.

6.2 Improved limits of detection on the silica structures

Since it is of interest to use the SiO_2 structures as a sensing platform, it was important to assess detection sensitivity of the surface of this model-linking system. The detection sensitivity of the PO-SiO_2 substrates was evaluated by performing a concentration curve of STRITC on the PO-SiO_2 and glass substrate. The biotin-streptavidin hybridization was used since this system can be applied towards real immunoassays through DNA, protein, or aptamer linking.[123] The results are plotted in **Figure 6.1**. The fluorescence signal corresponding to the LOD is defined to be the mean of the background plus three times the standard deviation of the background. The LOD is calculated to be an applied STRITC concentration of 0.26 μg mL^{-1} (SE = 0.026) on the heated glass surface. In contrast, the shrunk PO-SiO_2 substrate is able to yield a lower LOD of STRITC concentration of 11 ng mL^{-1} (SE =

0.0027). This proof-of-concept demonstrates that the PO-SiO_2 substrate has higher detection sensitivity relative to planar glass surface. The ability to reach lower limits of detection using the biotin-streptavidin model linking system is promising as it suggested the possibility for applications in disease diagnostics and point-of-care testing.

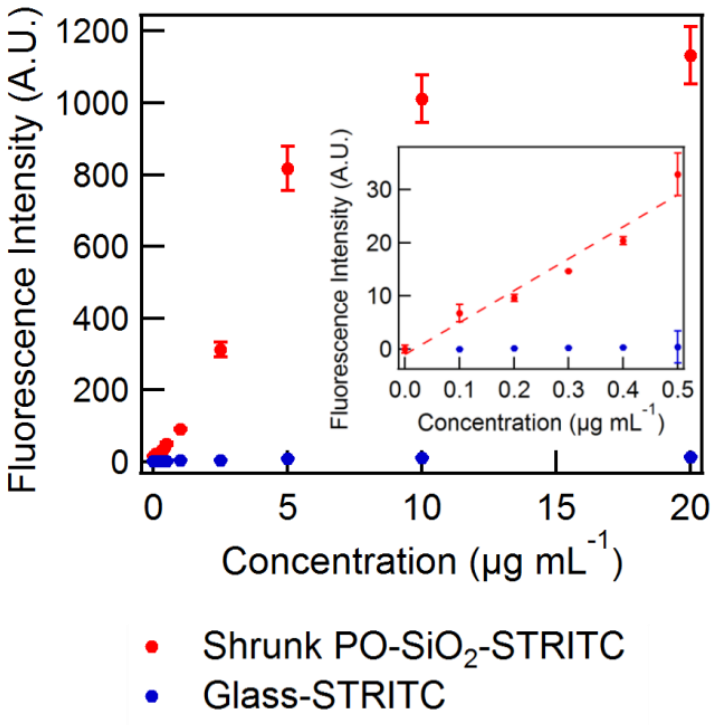

Figure 6.1. A plot of the fluorescence intensity as a function of STRITC concentration on the shrunk PO-SiO_2 substrate and the glass surface. The inset graph is a zoom of the lower STRITC concentrations, background subtracted for each respective substrate.

6.3 TNF-α detection

Tumor necrosis factor α (TNF-α) are pro-inflammatory cytokines secreted by macrophages and monocytes in response to inflammation, stresses and infection. TNF-α exist at sub-pM level in healthy individuals but are elevated by several orders of magnitude in patients with diseases such as in preeclampsia[130] and sepsis.[131] TNF-α also plays a role in regulating disease inflammation and progression.[132,133] It is important to be able to detect

and quantify the low levels of TNF-α as TNF-α could represent an early stage indicator of systemic infection. The gold standard for protein detection is the enzyme-linked immunosorbent assay (ELISA). However, the limit of detection (2 pgmL^{-1}) fails to capture protein levels associated with early inflammation and infection. Here we develop a sandwich immunoassay to detect human TNF-α using the SiO_2 structures.

Instead of covalently linking the capture antibody onto the SiO_2 films, we tested adsorption as a method for depositing the capture protein. First, we chemically functionalized the unshrunk SiO_2 film (20 nm SiO_2) with APTMS (2% v/v) for 30 min to introduce primary amine groups. The slight hydrophobicity increases protein affinity. Following APTMS treatment, the surfaces were rinsed and incubated overnight with monoclonal mouse TNF-α antibody (25 μg mL^{-1}). The capture antibody was removed, surfaces were washed, and blocked with StartingBlock buffer. Varying concentrations of target analyte TNF-α were incubated with the surface overnight, and detected the next day using rabbit polyclonal anti TNF-α antibody (1 μg mL^{-1}). Goat anti-rabbit IgG H&L (Alexafluor 647) (2 μg mL^{-1}) was then incubated for fluorescence visualization of the detected TNF-α. The functionalized films were shrunk thermally and imaged with an upright fluorescence microscope using a 5x objective (NA = 0.13, Olympus).

The results from the TNF-α immunoassay are shown in **Figure 6.2**. The concentration curve for TNF-α on the SiO_2 structures is compared to that on a planar glass surface. Both surfaces were heat treated, and higher fluorescence intensities were found on the SiO_2 substrates (as expected). The LOD, calculated to be three times the standard deviation above the background, on the SiO_2 structures is 550 pg mL^{-1} compared to that of 2.5 ng mL^{-1} on the glass surface. Lower LODS are reached on the SiO_2 structures, however it is noted that the

performance of the TNF-α immunoassay still falls short from the gold standard ELISA assay. This could be due to relying on adsorption as the main means of binding capture antibody to the surface. Protein adsorption to the surface may result in irreversible protein denaturing and subsequent loss of active sites.[134] Many circumstances such as antibody affinity, activity, and selectivity need to be taken into consideration when developing an immunoassay. Furthermore, ELISA well plates are gamma irradiated for strong protein adhesion. Oxygen plasma treatment and silane chemistry may not provide a strong enough adhesion layer for the captured antibody.

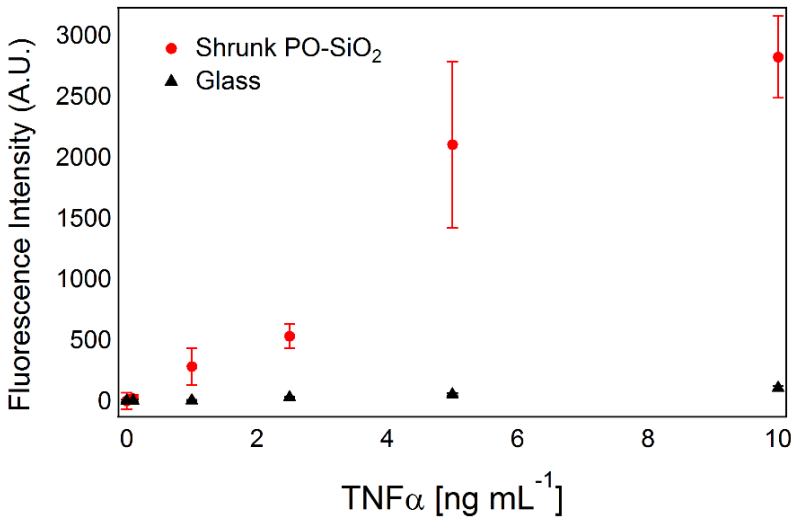

Figure 6.2. A graph of the fluorescence intensity detected per concentration of TNF-α, where the fluorescence intensity on the glass substrate is represented by the black triangles, and the fluorescence intensity on the shrunk PO-SiO_2 is represented by the red circles.

6.4 p24 detection

Human immunodeficiency virus type 1 (HIV-1) is a lentivirus that causes HIV infection. If left untreated, HIV eventually leads to acquired immunodeficiency syndrome (AIDS). According to UNAID, at the end of 2014 approximately 36.9 million people worldwide are living with HIV, with approximately 77% of these HIV cases reported to occur

in sub-Saharan Africa. Since 2000, 25.3 million people have died from AIDS-related illnesses.[135] HIV-1 diagnosis is essential for treating, monitoring, and preventing further transmission of the virus. The most common test for HIV-1 involves detection of HIV-1 antibodies using the conventional ELISA and more recently rapid diagnostic tests (RDTs). However, antibodies for HIV-1 are only detectable in blood 3-4 weeks after infection, leaving a window of opportunity for further transmission of the virus. The timeline of HIV-1 onset and appearance of biomarkers indicative of the HIV-1 infection are shown in **Figure 6.3**.

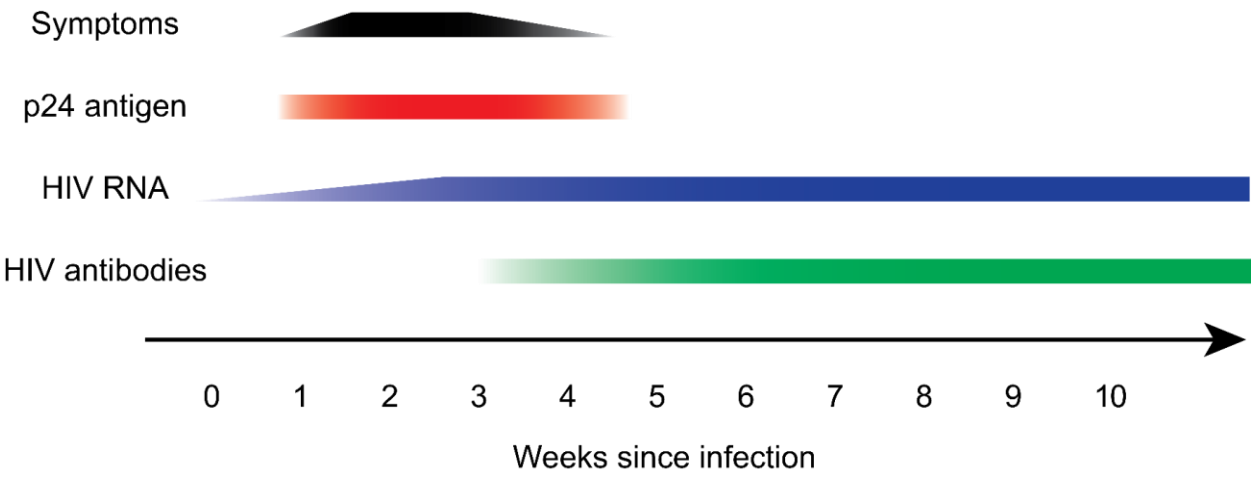

Figure 6.3. The timeline shows onset of HIV-1 and corresponding biomarkers that become present in the body.

The nucleocapsid protein p24 antigen is a marker for HIV-1. It presents itself in the infected individual during the acute infection stage, and therefore is a useful target for early detection of HIV-1 while antibody concentrations within the body is low.[136–138] We look to develop an immunoassay for p24 detection on the SiO_2 structures. Previously, we demonstrated improved LOD of TNF-α on our substrates, however detection capability fell slightly short of that reachable on the gold standard ELISA. Here, we describe a new

approach where we covalently link the capture antibody to potentially improve its binding efficiency and become a competitive immunoassay.

The immunoassay scheme is shown in **Figure 6.4**. We crosslinked the SiO_2 surfaces (20 nm SiO_2) with APTMS (2 % v/v) for 30 min. The surfaces were rinsed, cured overnight, and then incubated with pGlu (3 mg mL^{-1}) for 1 h at room temperature the next day. After washing with ddH_2O, the substrates were incubated in EDC-HCl/Sulfo-NHS (75 mM/15mM) solution for 1 h for protein crosslinking. 10 μg mL^{-1} of monoclonal mouse anti-HIV1 p24 antibody was conjugated onto the EDC-HCl/Sulfo-NHS activated surfaces by incubating the protein solution with the surfaces overnight at 4 ˚C. Surfaces were washed with 0.05 % v/v PBST three times the next day to remove excess antibodies and blocked with StartingBlock. Human HIV-1 p24 antigen was incubated with the surfaces overnight at 4 ˚C. Following capture of the target analyte, polyclonal rabbit anti-HIV1 p24 antibody was incubated with the surface for antigen-antibody recognition. Hybridization of goat anti-rabbit IgG H&L (Alexa Fluor 647) to the polyclonal rabbit anti-HIV1 p24 antibody was performed for final visualization of the p24 antigen. The primary and secondary antibody binding was carried out at 37 ˚C for 1 h. After the substrates were cleaned, the films were thermally shrunk at T = 145 ˚C, and wide-field fluorescence intensity images were taken using 5x objective (NA = 0.13, Olympus).

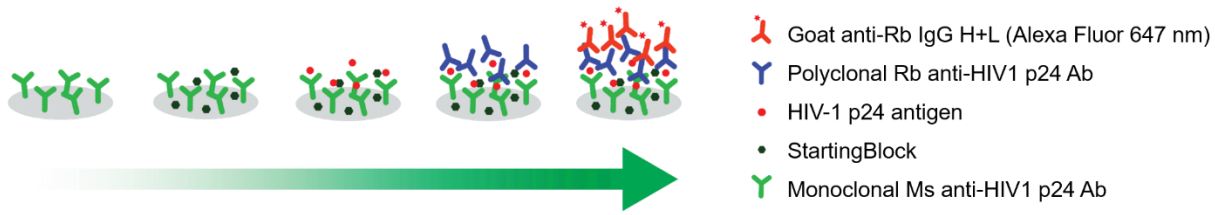

Figure 6.4. Schematic illustrating the p24 sandwich immunoassay performed on the SiO_2-coated film prior to shrinkage. After incubation with the secondary antibody, the entire substrate is shrunk and imaged using an upright epifluorescence microscope.

The results are shown in **Figure 6.5**, which is a concentration curve of the fluorescence intensity as a function of HIV-1 p24 antigen concentration. The LOD is determined at 3 standard deviations above the background, and we observed an improved LOD on the SiO_2 structures (30 pg mL^{-1}) over the planar glass substrate (253 pg mL^{-1}). 10 pg mL^{-1} of p24 was reported to be detectable through ELISA.[139] We anticipate with surface chemistry optimization and improvement of the reflective nature of our SiO_2 structures, our p24 assay platform will be able to surpass limits obtained using the standard ELISA. Furthermore, the SiO_2 sensing platform offers the potential for multiplexing as we have demonstrated improved DNA hybridization assay performance on the SiO_2 structures.[140] As seen in **Figure 6.4**, other biomarkers such as HIV RNA and the antibodies specific to HIV arise in the body as the disease progresses. Therefore, the SiO_2 structures can not only be used to diagnose HIV during the acute infection stage, but also to serve as a versatile platform for both RNA and HIV antibody sensing following the acute infection stage. This is advantageous since traditional ELISA assays are limited to protein detection.

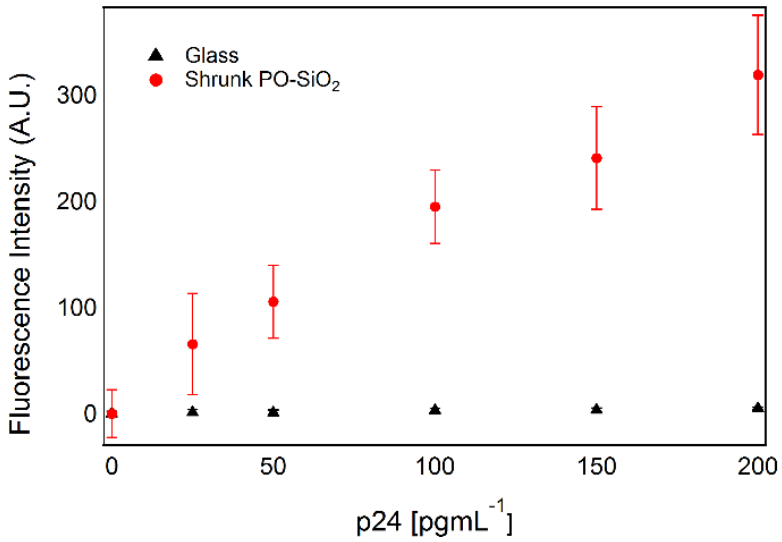

Figure 6.5. Illustration of fluorescence intensity dependence on p24 concentration, where data on the glass substrate are represented by the black triangles, and on the shrunk PO-SiO_2 are represented by the red circles. Improved LOD is achieved on the SiO_2 structures.

6.5 Summary

We first showed the SiO_2 structures are able to enhance the fluorescence signals of covalently conjugated model protein streptavidin-TRITC. This proof-of-concept indicated that the SiO_2 structures have potential to serve as a platform for disease diagnostics. Following this proof-of-concept, we applied the SiO_2 structures towards disease detection. We demonstrated that the SiO_2 structures were efficacious in disease diagnostic applications through detection of clinically relevant molecules TNF-α and HIV-1 p24 antigen. Lowered LOD of 550 pg mL^{-1} and 30 pg mL^{-1} for TNF-α and p24, respectively, were achieved on the SiO_2 structures. This is an improvement over the LOD of 2.5 ng mL^{-1} and 253 ng mL^{-1} for TNF-α and p24, respectively, observed on the planar glass control. The ability to reach better LOD on the SiO_2 structures suggests their potential for applications in POC diagnostics.

CHAPTER 7: TOWARDS POINT-OF-CARE DEPLOYMENT

7.1 Translation towards point-of-care deployment

As mentioned in **Chapter 1**, this work aims to develop a POC applicable sensing surface for rapid, low cost detection of analytes. Up to now, we have demonstrated the fabrication of a fluorescence signal enhancing platform and shown the ability of the SiO_2 platform to yield improved limits of detection for target analytes. Translation of the SiO_2 structures towards a POC applicable platform requires additional work, and we present two avenues of exploration to further move the SiO_2-based fluorescence enhancing system towards POC deployment. These avenues are improving: 1. Cost and scalability via sol-gel derived silicate materials and 2. Portability through colorimetric detection.

7.1.1 Sol-gel chemistry

Ion beam sputter deposition was used for depositing SiO_2 thin films in this project. This expensive machinery contributes a substantial cost to this technology. Therefore, it is of interest to explore other avenues of SiO_2 thin film deposition for feasible integration of the SiO_2 structures into actual low-cost POC technologies.

Sol-gel processing is a wet deposition method for fabrication of silicate based materials at room temperature.[141,142] This process has been developed and expanded towards multiple applications in electronics, nanotechnology, chemistry, materials, and optics. Sol-gel processing involves the hydrolysis of silicon alkoxide precursors such as tetramethyoxysilane (TMOS) or tetraethoxysilane (TEOS) and polycondensation to yield a network of siloxane bonds.[143] The resulting silica-based matrix is physical robust, resistant to abrasion, chemically inert, displays optical transparency, and is thermally and chemically stable. These properties make the sol-gel

derived silicate materials ideal for biosensing applications. However, traditional sol-gel processing can be disadvantageous for protein encapsulation due to the need for an acidic medium to hydrolyze the silicate groups and the generation of alcohol groups during the hydrolysis reaction.[144]

Advancements in sol-gel chemistry have resulted in biocompatible sol-gel processing techniques. This involves the addition of glycerol or other small molecule "osmolytes" such as sugars and amino acids during the encapsulation process to improve protein stability, the use of biocompatible silane precursors such as polyglycerylsilicate (PGS), diglycerylsilane (DGS), sodium silicate (SS) to eliminate the alcohol production, and the use of sugar-modified silica materials.[145,146] Many reports of using sol-gel derived films for sensing surfaces have been reported using both biomolecule encapsulation during processing and postgrafting.[54,147–149,145,150,151,146] Synthesis of sol-gel materials involves hydrolysis of an appropriate precursor, e.g., to form an aqueous sol, during which the biomolecules is also added. Addition of various salts and catalysts polymerizes the gel, resulting in biomolecule entrapment if biomolecule addition took place.[152] Sol-gel processing for SiO_2 thin film deposition is explored as a low cost alternative for SiO_2 structure fabrication. SiO_2 sol-gels are synthesized as described by Carrasquilla, C. *et al.*[151]

7.1.2 Sol-gel based silica thin films

We use an aqueous, biofriendly sol-gel processing method described by Carrasquilla, C. *et al*. for the deposition of a SiO_2 thin film on the PO film.[151] Briefly, the SS solution was prepared by diluting 2.6 g of stock SS solution into 10 mL of ddH_2O. The solution was mixed with 5.5 g of cation resin (Dowex 50WX8, 100-200 mesh) to lower the pH to 4. The Dowex resin was removed and the SS solution is mixed at 1:1 (v/v) ratio with HEPES buffer.

Structure fabrication on the shrink film polymer is shown as seen in **Figure 7.1a**. The PO film is oxygen plasma treated for 5 min. The SS solution is spin-coated at 1500 rpm onto the surface of the treated film and allowed to cure overnight. SS sol-gel coated films henceforth will be referred to as PO-SS.

Atomic force microscopy (AFM) images of the PO film and the film after spin-coating SS sol-gel are shown in **Figure 7.1b**. The amplitude images indicate that the PO film alone has a softer surface. Upon coating with the SS, the PO-SS's surface became less elastic with increased uniformity. Thermal shrinkage of the PO-SS films resulted in wrinkle formation as seen in **Figure 7.1c**.

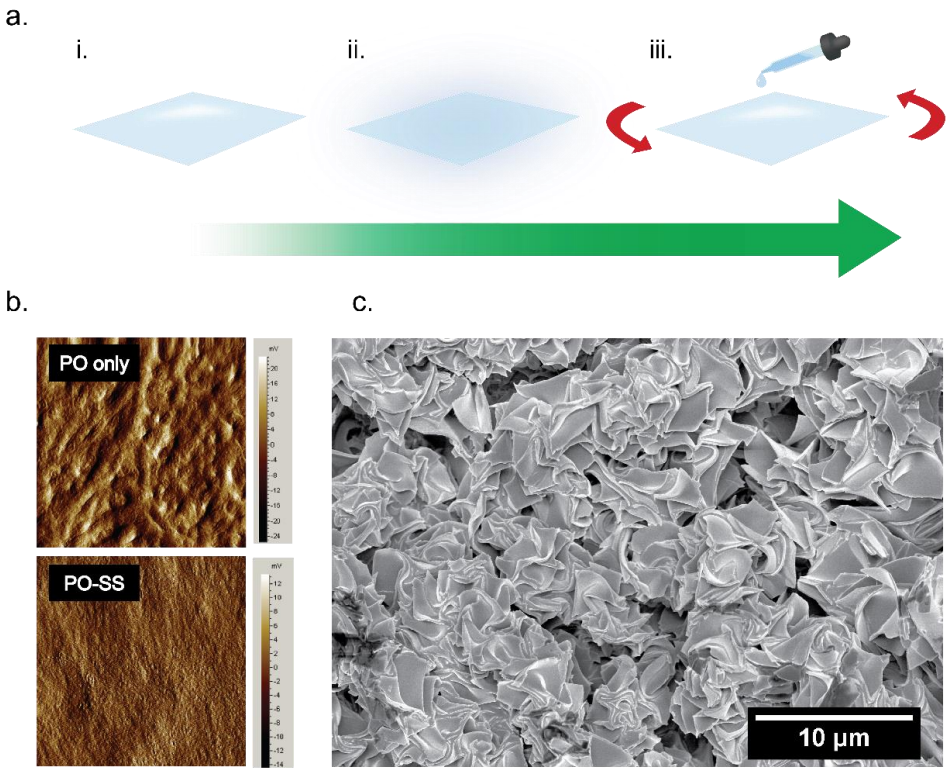

Figure 7.1 Schematic illustrating the use of sol-gel derived materials for SiO_2 thin film deposition (a). A clean PO film (i) is oxygen plasma treated to help with adhesion of the sol-gel film (ii). Sodium silicate sol-gel is spin coated onto the oxygen plasma treated PO film (iii). AFM microscopy shows SS sol-gel adhesion to the PO surface to change it's the film's surface properties (b). Thermal shrinkage of the PO-SS film results in the formation of sodium silicate SiO_2 wrinkles.

We show that the PO-SS is a suitable solid-phase platform for both protein encapsulation and protein post-grafting with two simple proof-of-concepts, whose results are shown in **Figure 7.2**. First we demonstrate protein encapsulation and subsequent binding to the target protein by mixing streptavidin in the SS solution at a 1:1 (v/v) ratio of 20 μg mL^{-1} of streptavidin (Jackson ImmunoResearch) diluted in HEPES. The streptavidin:SS mixture was spin-coated onto the PO surface and cured overnight. We reacted the surfaces with Atto 550-Biotin (Sigma) and observed binding as indicated by fluorescence. Shrinkage of the PO-SS substrates revealed similar levels of fluorescence SI (~58-fold). The PO-SS substrates are shown in **Figure 7.2a**.

Secondly, we use the SS solution as a platform for binding on the surface. The SS solution was mixed at 1:1 (v/v) ratio with HEPES buffer and spin-coated onto the surface. After curing overnight, the PO-SS films were oxygen plasma treated and submerged in (3-Glycidyloxypropyl)trimethoxysilane (2% v/v) to functionalize the surface with epoxy groups. 10 μg mL^{-1} monoclonal mouse IgG1 (Santa Cruz Biotechnology) was incubated with the surface overnight at 4 ˚C. The surface was rinsed and blocked with 1% BSA for 2 h, and then reacted with 10 μg mL^{-1} polyclonal goat anti-mouse IgG H&L (Alexafluor 555) for 1 h. Thermal shrinkage of the functionalized PO-SS surfaces, shown in **Figure 7.2b**, yielded a ~44-fold fluorescence SI.

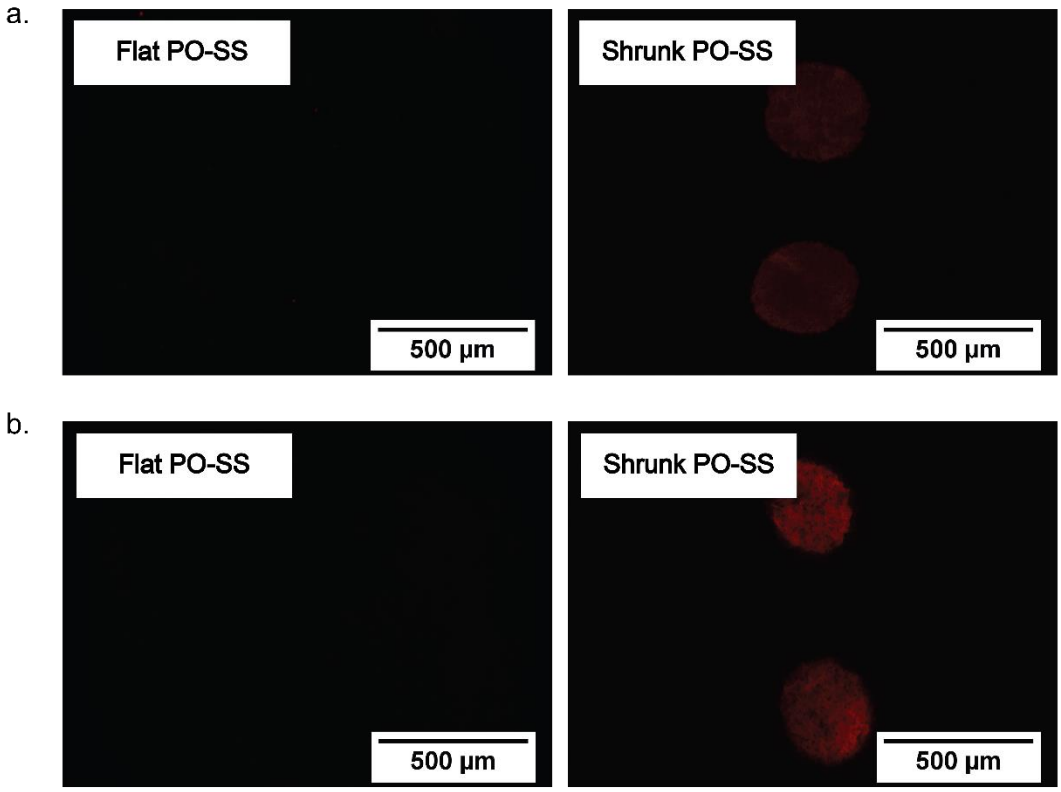

Figure 7.2 Fluorescence intensity images of the unshrunk and shrunk PO-SS surfaces. The PO-SS contain encapsulated streptavidin that is reacted with Atto 550-Biotin (a). The PO-SS surface is linked with monoclonal mouse antibody and visualized with goat anti-mouse IgG H&L (Alexa Fluor 555)

Further optimization and characterization of the SS sol-gels need to be performed for robustness and quality control. The ability to pattern discrete and homogeneous regions of SS is important for functionality as a consistent immunoassay platform.

7.1.3 Colorimetric detection on the silica substrates

The reported fluorescence SIs were quantified using a standard upright epifluorescence microscope. While it is less expensive than a confocal microscopy setup, a standard wide-field microscope may still require resources that are not consistently available in developing countries (where the predominant number of infectious disease

occur). It is of interest to develop an assay based off colorimetric readout methods on the SiO_2 structures render this system a truly simple, portable, and low-cost POC technology. For proof of concept, we look to use gold nanoparticles for colorimetric visualization. We leveraged the self-retracting properties of the shrink film polymer to concentrate the colorimetric signal of a simple immunoassay. 20 nm SiO_2 was sputtered onto clean PO film. The films were silane treated with APTMS (2% v/v) for 30 min, rinsed, and cured overnight. Glutaraldehyde (2.5% v/v) was used to crosslink monoclonal mouse IgG1 to the surface. Following removal of the primary antibody, the substrates were washed and blocked with StartingBlock. Biotinylated goat anti-mouse IgG (H&L) (10 µg mL^{-1}) was incubated for 1 h on the surface for detection of the mouse IgG, and the surfaces were hybridized with streptavidin conjugated 20 nm gold nanoparticles for 1 h (1:50 dilution). GoldEnhance (Nanoprobes), was applied for 25 min to enlarge the gold nanoparticles and for visualization. The schematic is illustrated in **Figure 7.3**.

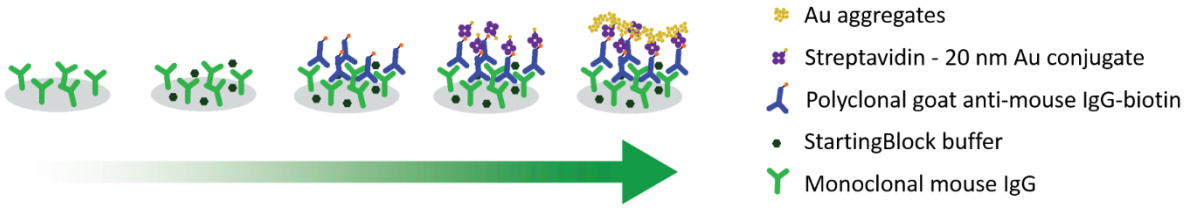

Figure 7.3. Schematic illustrating the immunoassay for colorimetric detection. Monoclonal mouse IgG is crosslinked onto the SiO_2 surface. Surfaces are blocked with StartingBlock, incubated with polycloncal goat anti-mouse IgG-biotin, and reacted with streptavidin-Au nanoparticle conjugate. GoldEnhance is applied for gold nanoparticle enlargement. Substrates are then shrunk and imaged.

The surfaces were imaged using an upright digital microscope (Keyence, VHX-5000) as shown in **Figure 7.4**. Image analysis was done using MATLAB and the blue channel of region-of-interest (ROI) was quantified for changes in signal. A concentration curve for the

lowest detectable amount of monoclonal mouse IgG was performed and the results are shown in **Figure 7.5**. The simple immunoassay demonstrated sigmoidal behavior, with a shift to higher colorimetric readout per mouse monoclonal IgG concentration on the shrunk PO-SiO_2 surfaces. An improved LOD of monoclonal mouse IgG was achieved on the SiO_2 structures. The LOD, calculated as the value higher than three times the standard deviation of the background, was calculated to be 18 pg mL^{-1} on the SiO_2 structures and 92.4 pg mL^{-1} on glass.

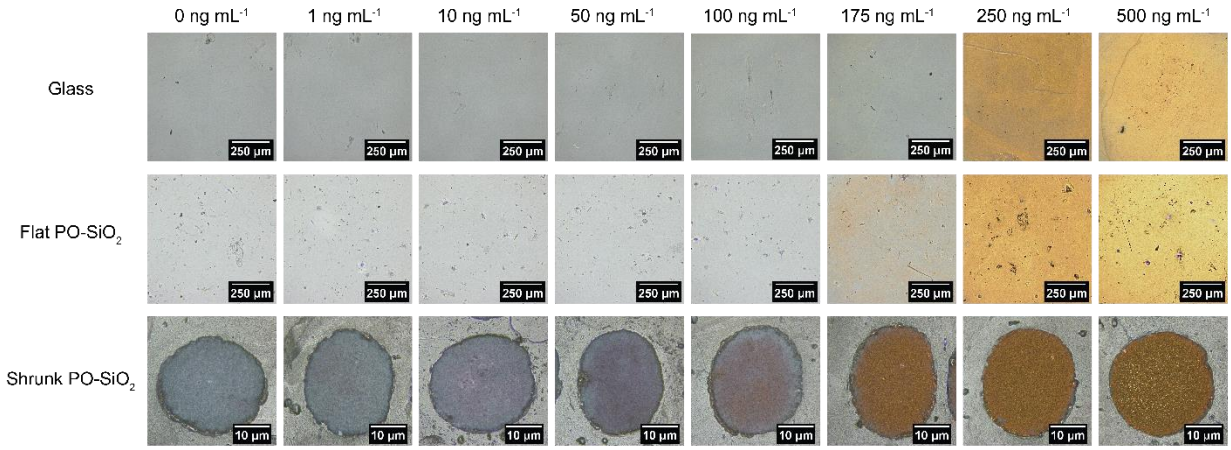

Figure 7.4 Images of the functionalized surfaces with different concentrations of monoclonal mouse IgG (0 – 500 ng mL^{-1}).

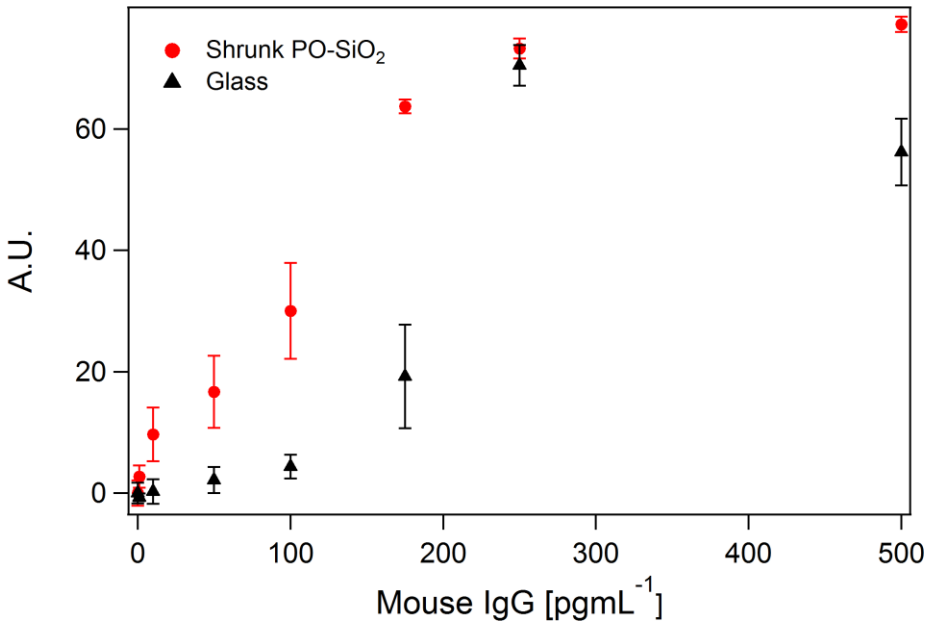

Figure 7.5 A concentration curve of the colorimetric signal per concentration of monoclonal mouse IgG on the SiO_2 structures (indicated by the red spots) and the glass surface (indicated by the black triangles).

The improved LOD achievable on the SiO_2 structures using the simple model immunoassay suggests the potential of the shrink-derived SiO_2 structures as a successful platform for colorimetric-based diagnostics. We are interested in demonstrating improved detection capabilities of an actual infectious agent using colorimetric readout methods.

CHAPTER 8: SUMMARY AND FUTURE WORKS

8.1 Summary of the work

In this work, we described a platform for disease detection with wrinkled surfaces from conception to application. Tunable multiscale micro- to nano- SiO_2 wrinkle structures were fabricated using the shrink technology with simple top-down approaches (Chapter 3). Structure functionalization and robust, far-field fluorescence signal enhancements (SI of ~116-fold and EF of ~50-fold) with improved SNRs were reported (Chapter 4). Optical characterization of the SiO_2 structures revealed the SiO_2 structures to be highly scattering. This is the main contributor (along with increased surface density) to the fluorescence signal enhancements seen on the SiO_2 structures (Chapter 5). Sensitive and accurate diagnosis of infectious diseases is the driving motivator behind this work, and we demonstrated applicability of our SiO_2 substrates with improved detection of TNF-α and p24 antigen (Chapter 6). Work done to further translate the SiO_2 technology towards actual point-of-care applications regarding: 1. Cost and scalability via sol-gel derived silicate materials and 2. Portability through colorimetric detection were presented (Chapter 7).

8.2 Concluding remarks

The work presented in this dissertation focuses on developing a robust and deployable platform for disease diagnostic applications. The SiO_2 technology described in this work is a promising sensing platform, though work still needs be done to improve this technology to render it truly portable and effective for low resource settings. Work important for translation of the SiO_2 technology towards deployable POC diagnostics include finding a more cost effective way for creating SiO_2 thin films on the shrink film polymer,

lowering the background to improve the SNR, and moving the system to support colorimetric readout methods. We have shown preliminary data regarding those areas, but continual efforts are needed for further development of the technology. Additional efforts to move of the SiO_2 platform towards a field- or clinical lab- appropriate technology include using a low temperature polymer shrink film and a more reflective material for increased optical scattering. A low temperature polymer shrink film would enable users to shrink, or create the micro- to nanostructures at lower temperatures, eliminating the concern of denaturing proteins and potentially allowing analysis of captured analytes. The use of a more reflective thin film, or combining another material with the SiO_2 thin film to increase the reflectivity, could potentially allow for more optical scattering, thereby improving the detection capability of the SiO_2 structures. Further work is required to explore this idea.

Overall, the SiO_2 technology represents a promising platform for sensing applications. The SiO_2 structures are simple to fabricate and eliminate many processing steps associated with traditional nanostructure fabrication methods. We are able to pattern on a large scale and then shrink to create the SiO_2 structures that yield robust, far-field fluorescence signal enhancements. These structures are promising as the fluorescence enhancements effects are not limited to the near-field and are wavelength independent. Furthermore, the SiO_2 technology supports different assay types as both improved detection of DNA and protein have been demonstrated. This potentially allows for the development of multiplexed assays with different target molecules of interest. We have shown the ability to deposit silver and calcium thin films which is amenable to roll-to-roll manufacturing for fabrication of micro- and nanostructures.[153] By moving the processing of SiO_2 thin films onto the shrink film polymer to large-scale, we bring the SiO_2 technology closer towards a POC sensing platform.

REFERENCES

(1) Fauci, A. S.; Morens, D. M. *N. Engl. J. Med.* **2012**, *366* (5), 454–461.

(2) Morens, D. M.; Folkers, G. K.; Fauci, A. S. *Nature* **2004**, *430* (6996), 242–249.

(3) Gupta, E.; Bhalla, P.; Khurana, N.; Singh, T. *Indian J. Med. Microbiol.* **2009**, *27* (2), 100–106.

(4) Mabey, D.; Peeling, R. W.; Ustianowski, A.; Perkins, M. D. *Nat. Rev. Microbiol.* **2004**, *2* (3), 231–240.

(5) Pérez-Luna, V. H.; O'Brien, M. J.; Opperman, K. a.; Hampton, P. D.; López, G. P.; Klumb, L. a.; Stayton, P. S. *J. Am. Chem. Soc.* **1999**, *121* (27), 6469–6478.

(6) Bissonnette, L.; Bergeron, M. G. *J. Pers. Med.* **2012**, *2* (2), 50–70.

(7) Bissonnette, L.; Bergeron, M. G. *Clin. Microbiol. Infect.* **2010**, *16* (8), 1044–1053.

(8) Yager, P.; Domingo, G. J.; Gerdes, J. *Annu. Rev. Biomed. Eng.* **2008**, *10*, 107–144.

(9) World Bank. *World Development Report 2004: Making services work for poor people*; 2004.

(10) Gubala, V.; Harris, L. F.; Ricco, A. J.; Tan, M. X.; Williams, D. E. *Anal. Chem.* **2012**, *84* (2), 487–515.

(11) Peeling, R. W.; Mabey, D. *Clin. Microbiol. Infect.* **2010**, *16* (8), 1062–1069.

(12) Lakowicz, J. R. *Principles of fluorescence spectroscopy*; 2006.

(13) Tsien, R. Y. *Biochemistry* **1980**, *19* (1966), 2396–2404.

(14) Grynkiewicz, G.; Poenie, M.; Tsien, R. Y. *J. Biol. Chem.* **1985**, *260* (6), 3440–3450.

(15) Chandrasekaran, A.; Acharya, A.; You, J. L.; Soo, K. Y.; Packirisamy, M.; Stiharu, I.; Darveau, A. *Sensors* **2007**, *7* (9), 1901–1915.

(16) Steemers, F. J.; Ferguson, J. a; Walt, D. R. *Nat. Biotechnol.* **2000**, *18*, 91–94.

(17) Sousa-Figueiredo, J. C.; Oguttu, D.; Adriko, M.; Besigye, F.; Nankasi, A.; Arinaitwe, M.; Namukuta, A.; Betson, M.; Kabatereine, N. B.; Stothard, J. R. *Malar. J.* **2010**, *9*, 245.

(18) Woodbury, R. L.; Varnum, S. M.; Zangar, R. C. *J. Proteome Res.* **2002**, *1* (3), 233–237.

(19) Turner, L.; Ryu, W. S.; Berg, H. C. *J. Bacteriol.* **2000**, *182* (10), 2793–2801.

(20) Kremers, G.; Gilbert, S. G.; Cranfill, P. J.; Davidson, M. W.; Piston, D. W. *J. Cell Sci.* **2011**, *124* (Pt 2), 157–160.

(21) Ghosh, K. K.; Burns, L. D.; Cocker, E. D.; Nimmerjahn, A.; Ziv, Y.; Gamal, A. El; Schnitzer, M. J. *Nat. Methods* **2011**, *8* (10), 871–878.

(22) Miller, A. R.; Davis, G. L.; Oden, Z. M.; Razavi, M. R.; Fateh, A.; Ghazanfari, M.; Abdolrahimi, F.; Poorazar, S.; Sakhaie, F.; Olsen, R. J.; Bahrmand, A. R.; Pierce, M. C.; Graviss, E. a; Richards-Kortum, R. *PLoS One* **2010**, *5* (8), e11890.

(23) Altman, R. B.; Terry, D. S.; Zhou, Z.; Zheng, Q.; Geggier, P.; Kolster, R. a; Zhao, Y.; Javitch, J. a; Warren, J. D.; Blanchard, S. C. *Nat. Methods* **2011**, *9* (1), 68–71.

(24) Panchuk-Voloshina, N.; Haugland, R. P.; Bishop-Stewart, J.; Bhalgat, M. K.; Millard, P. J.; Mao, F.; Leung, W. Y.; Haugland, R. P. *J. Histochem. Cytochem.* **1999**, *47* (9), 1179–1188.

(25) Petty, H. R. *Microsc. Res. Tech.* **2007**, *70* (8), 687–709.

(26) Pokhriyal, A.; Lu, M.; Chaudhery, V.; Huang, C.-S.; Schulz, S.; Cunningham, B. T. *Opt. Express* **2010**, *18* (24), 24793–24808.

(27) Pompa, P. P.; Martiradonna, L.; Torre, a Della; Sala, F. Della; Manna, L.; De Vittorio, M.; Calabi, F.; Cingolani, R.; Rinaldi, R. *Nat. Nanotechnol.* **2006**, *1* (2), 126–130.

(28) Diebold, E. D.; Mack, N. H.; Doorn, S. K.; Mazur, E. *Langmuir* **2009**, *25* (3), 1790–1794.

(29) Bohren, C. F.; Huffman, D. R. *Absorption and scattering of light by small particles*; 1983; Vol. 1.

(30) Bauch, M.; Toma, K.; Toma, M.; Zhang, Q.; Dostalek, J. *Plasmonics*. 2013, pp 1–19.

(31) Willets, K. A.; Van Duyne, R. P. *Annu. Rev. Phys. Chem.* **2007**, *58*, 267–297.

(32) Darvill, D.; Centeno, A.; Xie, F. *Phys. Chem. Chem. Phys.* **2013**, *15*, 15709–15726.

(33) Zang, J.; Fu, Y.; Liang, D.; Zhao, R. Y.; Lakowicz, J. R. *Langmuir* **2008**, *24* (21), 12452–12457.

(34) Zhou, L.; Ding, F.; Chen, H.; Ding, W.; Zhang, W.; Chou, S. Y. *Anal. Chem.* **2012**, *84* (10), 4489–4495.

(35) Corrigan, T. D.; Guo, S.; Phaneuf, R. J.; Szmacinski, H. *J. Fluoresc.* **2005**, *15* (5), 777–784.

(36) Geddes, C. D.; Parfenov, A.; Roll, D.; Fang, J.; Lakowicz, J. R. *Langmuir* **2003**, *19* (15), 6236–6241.

(37) Geddes, C. D.; Parfenov, A.; Roll, D.; Gryczynski, I.; Malicka, J.; Lakowicz, J. R. *Journal of Fluorescence*. 2003, pp 267–276.

(38) Shtoyko, T.; Matveeva, E. G.; Chang, I. F.; Gryczynski, Z.; Goldys, E.; Gryczynski, I. *Anal. Chem.* **2008**, *80* (6), 1962–1966.

(39) Zhang, J.; Fu, Y.; Chowdhury, M. H.; Lakowicz, J. R. *Nano Lett.* **2007**, *7* (7), 2101–2107.

(40) Kinkhabwala, A.; Yu, Z.; Fan, S.; Avlasevich, Y.; Müllen, K.; Moerner, W. E. *Nat. Photonics* **2009**, *3* (11), 654–657.

(41) Corrigan, T. D.; Guo, S. H.; Szmacinski, H.; Phaneuf, R. J. *Appl. Phys. Lett.* **2006**, *88* (10).

(42) Chou, S. Y.; Krauss, P. R.; Renstrom, P. J. *J. Vac. Sci. Technol. B Microelectron. Nanom. Struct.* **1996**, *14* (6), 4129.

(43) Das, G.; Battista, E.; Manzo, G.; Causa, F.; Netti, P. A.; Di Fabrizio, E. *ACS Appl. Mater. Interfaces* **2015**, *7* (42), 23597–23604.

(44) Acikgoz, C.; Hempenius, M. A.; Huskens, J.; Vancso, G. J. *Eur. Polym. J.* **2011**, *47* (11), 2033–2052.

(45) Xie, F.; Centeno, A.; Ryan, M. R.; Riley, D. J.; Alford, N. M. *J. Mater. Chem. B* **2013**, *1*, 536.

(46) Xie, F.; Pang, J. S.; Centeno, A.; Ryan, M. P.; Riley, D. J.; Alford, N. M. *Nano Res.* **2013**, *6* (7), 496–510.

(47) Slowing, I. I.; Vivero-Escoto, J. L.; Wu, C.-W.; Lin, V. S.-Y. *Adv. Drug Deliv. Rev.* **2008**, *60* (11), 1278–1288.

(48) Wang, K.; He, X.; Yang, X.; Shi, H. *Acc. Chem. Res.* **2013**, *46* (7), 1367–1376.

(49) Ma, Q.; Li, Y.; Su, X. *TrAC Trends Anal. Chem.* **2015**, *74*, 130–145.

(50) Flounders, a. W.; Singh, a. K.; Volponi, J. V.; Carichner, S. C.; Wally, K.; Simonian, a. S.; Wild, J. R.; Schoeniger, J. S. *Biosens. Bioelectron.* **1999**, *14*, 715–722.

(51) Grant, S.; Weilbaecher, C.; Lichlyter, D. *Sensors Actuators B Chem.* **2007**, *121* (2), 482–489.

(52) Wu, Y.; Chen, C.; Liu, S. *Anal. Chem.* **2009**, *81* (4), 1600–1607.

(53) Wang, L.; Zhao, W.; Tan, W. *Nano Res.* **2008**, *1* (2), 99–115.

(54) Monton, M. R. N.; Forsberg, E. M.; Brennan, J. D. *Chem. Mater.* **2012**, *24* (5), 796–811.

(55) Blaaderen, a Van; Vrij, a. *Langmuir* **1992**, *8* (12), 2921–2931.

(56) Verhaegh, N. a M.; Blaaderen, A. Van. *Langmuir* **1994**, *10* (9), 1427–1438.

(57) Graf, C.; Schartl, W.; Fischer, K.; Hugenberg, N.; Schmidt, M. *Langmuir* **1999**, *15*, 6170–6180.

(58) Gilliland, J. W.; Yokoyama, K.; Yip, W. T. *Chem. Mater.* **2005**, *17* (26), 6702–6712.

(59) Herz, E.; Ow, H.; Bonner, D.; Burns, A.; Wiesner, U. *J. Mater. Chem.* **2009**, *19* (35), 6341.

(60) Ow, H.; Larson, D. R.; Srivastava, M.; Baird, B. a.; Webb, W. W.; Wiesnert, U. *Nano Lett.* **2005**, *5* (1), 113–117.

(61) Larson, D. R.; Ow, H.; Vishwasrao, H. D.; Heikal, A. A.; Wiesner, U.; Webb, W. W.; Park, U. V; Pennsyl, V. *Chem. Mater.* **2008**, *20* (8), 2677–2684.

(62) Ma, D.; Kell, A. J.; Tan, S.; Jakubek, Z. J.; Simard, B. *J. Phys. Chem. C* **2009**, *113*, 15974–15981.

(63) Toptygin, D.; Savtchenko, R. S.; Meadow, N. D.; Roseman, S.; Brand, L. *J. Phys. Chem. B* **2002**, *106*, 3724–3734.

(64) Montalti, M.; Prodi, L.; Zaccheroni, N.; Battistini, G.; Marcuz, S.; Mancin, F.; Rampazzo, E.; Tonellato, U. *Langmuir* **2006**, *22* (13), 5877–5881.

(65) Rampazzo, E.; Bonacchi, S.; Montalti, M.; Prodi, L.; Zaccheroni, N. *J. Am. Chem. Soc.*

2007, *129* (46), 14251–14256.

(66) Miletto, I.; Gilardino, A.; Zamburlin, P.; Dalmazzo, S.; Lovisolo, D.; Caputo, G.; Viscardi, G.; Martra, G. *Dye. Pigment.* **2010**, *84* (1), 121–127.

(67) Alberto, G.; Miletto, I.; Viscardi, G.; Caputo, G.; Latterini, L.; Coluccia, S.; Martra, G. *J. Phys. Chem. C* **2009**, *113* (50), 21048–21053.

(68) Herz, E.; Marchincin, T.; Connelly, L.; Bonner, D.; Burns, A.; Switalski, S.; Wiesner, U. *J. Fluoresc.* **2010**, *20* (1), 67–72.

(69) Cho, E. B.; Volkov, D. O.; Sokolov, I. *Small* **2010**, *6* (20), 2314–2319.

(70) Cohen, B.; Martin, C.; Iyer, S. K.; Wiesner, U.; Douhal, A. *Chem. Mater.* **2012**, *24*, 361–372.

(71) Alberto, G.; Caputo, G.; Viscardi, G.; Coluccia, S.; Martra, G. *Chem. Mater.* **2012**, *24*, 2792–2801.

(72) Liang, S.; Shephard, K.; Pierce, D. T.; Zhao, J. X. *Nanoscale* **2013**, *5* (19), 9365–9373.

(73) Lin, S.; Lee, E. K.; Nguyen, N.; Khine, M. *Lab Chip* **2014**, *14* (18), 3475–3488.

(74) Ota, S. *J. Chem. Inf. Model.* **1981**, *18* (1-2), 81–87.

(75) Hsiue, G.; Yeh, T. *J. Appl. Polym. Sci.* **1989**, *37*, 2803–2816.

(76) Francesco, A. De; Duckett, R. A. *Polymer (Guildf).* **2004**, *45*, 4297–4306.

(77) Morshedian, J.; Khonakdar, H. A.; Mehrabzadeh, M.; Eslami, H. *Adv. Polym. Technol.* **2003**, *22* (2), 112–119.

(78) Khonakdar, H. a.; Morshedian, J.; Mehrabzadeh, M.; Wagenknecht, U.; Jafari, S. H. *Eur. Polym. J.* **2003**, *39*, 1729–1734.

(79) Nguyen, D.; Taylor, D.; Qian, K.; Norouzi, N.; Rasmussen, J.; Botzet, S.; Lehmann, M.; Halverson, K.; Khine, M. *Lab Chip* **2010**, *10* (12), 1623–1626.

(80) Bowden, N.; Brittain, S.; Evans, A. *Nature* **1998**, *393* (May), 146–149.

(81) Efimenko, K.; Rackaitis, M.; Manias, E.; Vaziri, A.; Mahadevan, L.; Genzer, J. *Nat. Mater.* **2005**, *4* (April), 293–297.

(82) Stafford, C. M.; Harrison, C.; Beers, K. L.; Karim, A.; Amis, E. J.; VanLandingham, M. R.; Kim, H.-C.; Volksen, W.; Miller, R. D.; Simonyi, E. E. *Nat. Mater.* **2004**, *3* (8), 545–550.

(83) Regehr, K. J.; Domenech, M.; Koepsel, J. T.; Carver, K. C.; Ellison-Zelski, S. J.; Murphy, W. L.; Schuler, L. A.; Alarid, E. T.; Beebe, D. J. *Lab Chip* **2009**, *9* (15), 2132–2139.

(84) Toepke, M. W.; Beebe, D. J. *Lab Chip* **2006**, *6* (12), 1484–1486.

(85) Fu, C. C.; Grimes, A.; Long, M.; Ferri, C. G. L.; Rich, B. D.; Ghosh, S.; Ghosh, S.; Lee, L. P.; Gopinathan, A.; Khine, M. *Adv. Mater.* **2009**, *21*, 4472–4476.

(86) Chen, A.; Lieu, D. K.; Freschauf, L.; Lew, V.; Sharma, H.; Wang, J.; Nguyen, D.; Karakikes, I.; Hajjar, R. J.; Gopinathan, A.; Botvinick, E.; Fowlkes, C. C.; Li, R. a.; Khine,

M. *Adv. Mater.* **2011**, *23* (48), 5785–5791.

(87) Turner, W. S.; Wang, X.; Johnson, S.; Medberry, C.; Mendez, J.; Badylak, S. F.; McCord, M. G.; McCloskey, K. E. *J. Biomed. Mater. Res. B. Appl. Biomater.* **2012**, *100* (8), 2060–2072.

(88) Luna, J. I.; Ciriza, J.; Garcia-Ojeda, M. E.; Kong, M.; Herren, A.; Lieu, D. K.; Li, R. a; Fowlkes, C. C.; Khine, M.; McCloskey, K. E. *Tissue Eng. Part C. Methods* **2011**, *17* (5), 579–588.

(89) Greco, F.; Fujie, T.; Ricotti, L.; Taccola, S.; Mazzolai, B.; Mattoli, V. *ACS Appl. Mater. Interfaces* **2013**, *5* (3), 573–584.

(90) Wang, J.; Chen, A.; Lieu, D. K.; Karakikes, I.; Chen, G.; Keung, W.; Chan, C. W.; Hajjar, R. J.; Costa, K. D.; Khine, M.; Li, R. a. *Biomaterials* **2013**, *34* (35), 8878–8886.

(91) Chen, A.; Lee, E.; Tu, R.; Santiago, K.; Grosberg, A.; Fowlkes, C.; Khine, M. *Biomaterials* **2014**, *35* (2), 675–683.

(92) Hatano, R.; Mercurio, K.; Luna, J. I.; Glaser, D. E.; Leppert, V. J.; McCloskey, K. E. *J. Biol. Eng.* **2013**, *7* (1), 18.

(93) Chen, C.-S.; Pegan, J.; Luna, J.; Xia, B.; McCloskey, K.; Chin, W.; Khine, M. *J. Vis. Exp.* **2008**, No. 13, 6–7.

(94) Nguyen, D.; Sa, S.; Pegan, J. D.; Rich, B.; Xiang, G.; McCloskey, K. E.; Manilay, J. O.; Khine, M. *Lab Chip* **2009**, *9* (23), 3338–3344.

(95) Lew, V.; Nguyen, D.; Khine, M. *J. Lab. Autom.* **2011**, *16* (6), 450–456.

(96) Chen, C.-S.; Breslauer, D. N.; Luna, J. I.; Grimes, A.; Chin, W.-C.; Lee, L. P.; Khine, M. *Lab Chip* **2008**, *8* (C), 622–624.

(97) Taylor, D.; Dyer, D.; Lew, V.; Khine, M. *Lab Chip* **2010**, *10* (18), 2472–2475.

(98) Grimes, A.; Breslauer, D. N.; Long, M.; Pegan, J.; Lee, L. P.; Khine, M. *Lab Chip* **2008**, *8* (1), 170–172.

(99) Chakraborty, A.; Xiang, M.; Luo, C. *Materials (Basel).* **2013**, *6* (8), 3610–3623.

(100) Nawarathna, D.; Norouzi, N.; McLane, J.; Sharma, H.; Sharac, N.; Grant, T.; Chen, A.; Strayer, S.; Ragan, R.; Khine, M. *Appl. Phys. Lett.* **2013**, *102* (6), 63504.

(101) Long, M.; Sprague, M. a.; Grimes, A. a.; Rich, B. D.; Khine, M. *Appl. Phys. Lett.* **2009**, *94* (13), 25–27.

(102) Pegan, J. D.; Ho, A. Y.; Bachman, M.; Khine, M. *Lab Chip* **2013**, *13* (21), 4205–4209.

(103) Greco, F.; Ventrelli, L.; Dario, P.; Mazzolai, B.; Mattoli, V. *Int. J. Hydrogen Energy* **2012**, *37* (22), 17529–17539.

(104) Zhang, B.; Cui, T. *J. Microelectromechanical Syst.* **2013**, *22* (5), 1140–1146.

(105) Liu, H.; Zhang, L.; Lang, X.; Yamaguchi, Y.; Iwasaki, H.; Inouye, Y.; Xue, Q.; Chen, M. *Sci. Rep.* **2011**, *1*, 112.

(106) Zhang, L.; Lang, X.; Hirata, A.; Chen, M. *ACS Nano* **2011**, *5* (6), 4407–4413.

(107) Liu, H.; Zhang, L.; Lang, X.; Yamaguchi, Y.; Iwasaki, H.; Inouye, Y.; Xue, Q.; Chen, M. *Sci. Rep.* **2011**, *1*, 1–5.

(108) Ross, B. M.; Wu, L. Y.; Lee, L. P. *Nano Lett.* **2011**, *11*, 2590–2595.

(109) Goff, G. Le. *Macromol. Biosci.* **2013**, *13* (2), 227–233.

(110) González, M.; Bagatolli, L. a.; Echabe, I.; Arrondo, J. L. R.; Argaraña, C. E.; Cantor, C. R.; Fidelio, G. D. *J. Biol. Chem.* **1997**, *272* (17), 11288–11294.

(111) Dundas, C. M.; Demonte, D.; Park, S. *Appl. Microbiol. Biotechnol.* **2013**, *97* (21), 9343–9353.

(112) Diamandis, E. P.; Christopoulos, T. K. *Clin. Chem.* **1991**, *37* (5), 625–636.

(113) Ye, L.; Pelton, R.; Brook, M. a. *Langmuir* **2007**, *23* (10), 5630–5637.

(114) Tannous, B. a; Grimm, J.; Perry, K. F.; Chen, J. W.; Weissleder, R.; Breakefield, X. O. *Nat. Methods* **2006**, *3* (5), 391–396.

(115) Tanaka, K.; Yokoi, S.; Morimoto, K.; Iwata, T.; Nakamoto, Y.; Nakayama, K.; Koyama, K.; Fujiwara, T.; Fukase, K. *Bioorg. Med. Chem.* **2012**, *20* (6), 1865–1868.

(116) Emerman, A. B.; Zhang, Z.-R.; Chakrabarti, O.; Hegde, R. S. *Mol. Biol. Cell* **2010**, *21* (24), 4325–4337.

(117) Skerra, a; Schmidt, T. G. *Methods Enzymol.* **2000**, *326* (FEBRUARY 2000), 271–304.

(118) Rodgers, J. T.; Patel, P.; Hennes, J. L.; Bolognia, S. L.; Mascotti, D. P. *Anal. Biochem.* **2000**, *277* (2), 254–259.

(119) Gruber, H. J.; Marek, M.; Schindler, H.; Kaiser, K. *Bioconjug. Chem.* **1997**, *8* (4), 552–559.

(120) Demirel, G.; Çaykara, T.; Akaoğlu, B.; Çakmak, M. *Surf. Sci.* **2007**, *601* (19), 4563–4570.

(121) Hoff, J. D.; Cheng, L. J.; Meyhöfer, E.; Guo, L. J.; Hunt, A. J. *Nano Lett.* **2004**, *4* (5), 853–857.

(122) Orth, R. N.; Clark, T. G.; Craighead, H. G. *Biomed. Microdevices* **2003**, *5* (1), 29–34.

(123) Bonanno, L. M.; Delouise, L. A. *Langmuir* **2007**, *23* (10), 5817–5823.

(124) Shalev, G.; Cohen, A.; Doron, A.; Machauf, A.; Horesh, M.; Virobnik, U.; Ullien, D.; Levy, I. *Sensors* **2009**, *9* (6), 4366–4379.

(125) Flink, S.; Van Veggel, F. C. J. M.; Reinhoudt, D. N. *J. Phys. Org. Chem.* **2001**, *14* (7), 407–415.

(126) Jung, L. S.; Nelson, K. E.; Stayton, P. S.; Campbell, C. T. *Langmuir* **2000**, *16* (9), 9421–9432.

(127) Gartia, M. R.; Eichorst, J. P.; Clegg, R. M.; Liu, G. L. *Appl. Phys. Lett.* **2012**, *101* (2).

(128) Del Monte, F.; Mackenzie, J. D.; Levy, D. *Langmuir* **2000**, *16* (19), 7377–7382.

(129) Dakin, John P., Brown, R. G. W. *Handbook of Optoelectronics*; Dakin, R., Ed.; Taylor & Francis: New York, 2006.

(130) Tarnowska-Madra, U.; Leibschang, J.; Kowalska, B.; Filipp, E.; Kozar, A.; Nimer, A.; Maciejewski, T. *Ginekol. Pol.* **2010**, *81* (3), 192–196.

(131) Cohen, J.; Abraham, E. *J Infect Dis* **1999**, *180* (1), 116–121.

(132) Wang, Y. Y.; Lo, G. H.; Lai, K. H.; Cheng, J. S.; Lin, C. K.; Hsu, P. I. *J. Chinese Med. Assoc. JCMA* **2003**, *66* (10), 593–598.

(133) Old, L. J. *Nature* **1987**, *326*, 330–331.

(134) Yakovleva, J.; Davidsson, R.; Lobanova, A.; Bengtsson, M.; Eremin, S.; Laurell, T.; Emnéus, J. *Anal. Chem.* **2002**, *74* (13), 2994–3004.

(135) *UNAID Fact Sheet 2015*; 2015.

(136) Dowbenko, D. J.; Bell, J. R.; Benton, C. V; Groopman, J. E.; Nguyen, H.; Vetterlein, D.; Capon, D. J.; Lasky, L. a. *Proc. Natl. Acad. Sci. U. S. A.* **1985**, *82* (November), 7748–7752.

(137) Clark, Stephen J., Saag, Michael S., Decker, Don W., Campbell-Hill, Sherri, Roberson, Joseph L., Veldkamp, Peter J., Kappes, JOhn C., Hahn, Beatrice H., Shaw, G. M. *N. Engl. J. Med.* **1991**, *324* (14), 954–960.

(138) Cohen, M. S.; Shaw, G. M.; McMichael, A. J.; Haynes, B. F. *N. Engl. J. Med.* **2011**, *364* (20), 1943–1954.

(139) Fan, P.; Li, X.; Su, W.; Kong, W.; Kong, X.; Wang, Z.; Wang, Y.; Jiang, C.; Gao, F. *PLoS One* **2015**, *10* (4), e0125701.

(140) Sharma, H.; Wood, J. B.; Lin, S.; Corn, R. M.; Khine, M. *Langmuir* **2014**, *30* (37), 10979–10983.

(141) Graham, T. *Proc. R. Soc. London* **1863**, *13*, 318–327.

(142) Kistler, S. S. *Rubber Chemistry and Technology*. 1932, pp 600–603.

(143) Walcarius, A.; Collinson, M. M. *Annu. Rev. Anal. Chem.* **2009**, *2*, 121–143.

(144) Klein, L. C. *Annu. Rev. Mater. Sci.* **1985**, *15* (1), 227–248.

(145) Bhatia, R. B.; Brinker, C. J.; Gupta, A. K.; Singh, A. K. *Chem. Mater.* **2000**, *12* (8), 2434–2441.

(146) Brennan, J. D. *Acc. Chem. Res.* **2007**, *40* (9), 827–835.

(147) Vanea, E.; Gruian, C.; Rickert, C.; Steinhoff, H. J.; Simon, V. *Biomacromolecules* **2013**, *14* (8), 2582–2592.

(148) Cruz-Aguado, J. a.; Chen, Y.; Zhang, Z.; Elowe, N. H.; Brook, M. a.; Brennan, J. D. *J. Am. Chem. Soc.* **2004**, *126* (22), 6878–6879.

(149) Carrasquilla, C.; Li, Y.; Brennan, J. D. *Anal. Chem.* **2011**, *83* (3), 957–965.

(150) Rupcich, N.; Nutiu, R.; Li, Y. F.; Brennan, J. D. *Anal. Chem.* **2005**, *77* (14), 4300–4307.

(151) Carrasquilla, C.; Lau, P. S.; Li, Y.; Brennan, J. D. *Journal of the American Chemical Society*. 2012, pp 10998–11005.

(152) Jin, W.; Brennan, J. D. *Anal. Chim. Acta* **2002**, *461* (1), 1–36.

(153) Nokes, J. M.; Liedert, R.; Kim, M.; Siddiqui, A.; Chu, M.; Lee, E.; Khine, M. **2015**, 1–25.